JOURNAL OF COMPUTATIONAL PHYSICS 77, 283–317 (1988)

Hypersonic, Stratified Gas Flows Past an Obstacle: Direct Simulation Monte Carlo Calculations

WILLIAM W. ROBERTS, JR.

Department of Applied Mathematics, University of Virginia,
Charlottesville, Virginia 22903

AND

MARK A. HAUSMAN

Mission Research Corporation, Santa Barbara, California 93106

Received October 30, 1985; revised August 11, 1987

Computational studies of the three-dimensional, hypersonic flow of rarefied, strongly stratified gas past an obstacle are carried out, the incident gas stratified in a direction transverse to the mean flow. An "N-body" computational code based on Monte Carlo techniques is developed for these purposes. Our primary interest is centered on the three-dimensional effects induced in the gas flow by a solid obstacle comparable in size to the gas scale height and collisional mean free path. Of the different types and shapes of obstacles studied, we focus herein on a cylindrical obstacle, assumed to be a diffuse elastic scatterer. The cylindrical obstacle is a short uniform pipe whose upstream end is fully open, facing directly into the flow, and whose downstream end is covered by a flat circular endplate containing an "orifice" at its center. For different choices of "orifice" diameter, the obstacle serves as a useful model of an impact probe (closed orifice) or scoop (closed, partially open, or fully open orifice) in a rapidly rotating strongly stratified gas (as in a gas centrifuge). The computed results show that the obstacle (in all cases studied, spanning the range from completely closed orifice to fully open orifice) induces large systematic motions in the gas, with strong radially inward driven flow in the direction of the gradient of density stratification, and correspondingly large density perturbations in these regions. The radial inflow of gas is prominent not only in the neighborhood of the obstacle and downstream from it but also at considerable distances radially inward from it and at z-heights well above and below. The radially driven gas inflow is a striking three-dimensional effect induced when strongly stratified gas impinges upon an obstacle; it constitutes a major characteristic common to all the hypersonic, stratified flows studied despite differences in Mach number and gas scale height and regardless of whether the obstacle is a flat plate, a "long" solid rod, or a "short" cylindrical pipe. The resultant density distribution of the obstructed molecular gas exhibits a striking "asymmetry" in the (radial) direction of the gradient of density stratification but retains "symmetry" in the z-direction perpendicular to the stratification gradient. The "r-asymmetry" is in striking contrast to the characteristic rotation-symmetry exhibited about the obstructing pipe's central axis in corresponding cases of unstratified flows investigated. The bow shock that forms near the obstacle exhibits a characteristic thickness that broadens with mean free path in the direction of the gradient of density stratification and a characteristic shape that is substantially warped (in that direction) from the paraboloid-shaped bow shock that forms (with axis of revolution

0021-9991/88 $3.00

coincident with the pipe's central axis) in corresponding cases of unstratified flows. The redirection of the gas flow at the shock away from the direction of the incident mean flow is particularly strong along that portion of the warped bow shock most closely aligned with the (radial) direction of the stratification gradient; the postshock density ridge in this direction is masked considerably by the strongly stratified density background.

I. INTRODUCTION

When simulating physical conditions in gaseous systems with rarefied or quasi-rarefied/continuum regimes, the familiar fluid equations (e.g., Navier–Stokes equations) are not very useful, because any small (computational) volume element will be influenced by all other elements within a few mean free paths in addition to the elements which border it. For such situations; an N-body particle method of computation is usually more useful. Our computational studies build upon Monte Carlo particle dynamics and, in particular, on the Direct Simulation Monte Carlo (DSMC) method described by Bird [1, 2]. In this method a gas is simulated by a number of particles, typically thousands to tens of thousands, each of which represents a very large number of identical gas molecules. By following the trajectories of these particles and determining the local averages of their number densities, velocities, and other properties throughout the computational volume, we may estimate the spatial variations of density, pressure, and mean velocity which would be exhibited by the gas. Each particle is subject to the same forces felt by a real molecule with the same location and velocity, colliding with other particles at the same rate as do real molecules.

In this work we shall use Monte Carlo particle dynamics to study the interaction of a stratified gas impinging hypersonically upon a solid body comparable in size to the gas scale height. The problem, difficult as it sounds, is made still more complicated by the fact that the collisional mean free path of the gas molecules is similar to the stratification scale length. Traditional methods of computing gas properties all fail in this regime. If the mean free path were much longer than the other relevant length scales., the gas could be treated as if it were collisionless and its properties calculated from the mean trajectories of noninteracting molecules. At the other limiting extreme, a dense gas with short mean free path could be treated by the traditional continuum fluid-dynamical equations. In the situation under consideration, however, it is necessary to use a computational method which takes into account both interactions between molecules and the smoothing effects induced by the long mean free path.

This problem has been little studied in part because there are not many natural situations in which this combination of parameters occurs. Rapidly rotating gas centrifuges, however, provide one practical and important situation where these particular relative length scales are achieved. In a gas centrifuge, the density scale height may be of order 1 cm, while the mean free path, much shorter at the wall, may increase to centimeter scales or greater near the center. When a solid object of similar size, such as an impact probe or scoop, is introduced into the rotor and held fixed in the laboratory frame, the hypothesized hypersonic relative velocities are readily attained.

In this paper, the intent is not to limit ourselves to gas centrifuge flows only. Rather we develop our Monte Carlo computational code with more general applicability; it is in this broader perspective that we describe our computational studies of three-dimensional hypersonic flows of rarefied, strongly stratified gas past an obstacle. Section II includes a general description of Monte Carlo particle dynamics and the computational code development necessary for application to rarefied, strongly stratified gas flows. Section III describes in some detail the results of our computational studies in two representative cases for which the obstacle adopted is a short, uniform, cylindrical pipe whose upstream end is fully open, facing directly into the flow, and whose downstream end is covered by a flat circular endplate containing an "orifice" at its center. For different choices of "orifice" diameter, this short cylindrical pipe serves as a useful model of an impact probe (closed orifice) or scoop (closed, partially open, or full-open orifice) in hypersonic, stratified gas flows. The two representative cases are those of "completely closed" orifice and "fully open" orifice, which together bound the full range of obstructed hypersonic, stratified gas flows of interest. We conclude in Section IV with a summary of the results for the hypersonic, stratified gas flows studied, a comparison with corresponding results for hypersonic, unstratified gas flows, and a discussion of their general applicability.

II. COMPUTATIONAL METHOD

The random component of Monte Carlo particle dynamics arises in the treatment of collisions. The frequency with which a single molecule in a simple, equilibrium gas collides with any other molecule is given by

$$\nu = n\overline{\sigma c_r} \equiv \bar{c}_r/(\sqrt{2}\,\lambda), \qquad (1)$$

where n is the molecular number density, c_r is the relative velocity between two molecules, σ is the collision cross section (which may be a function of c_r), λ is the mean free path, and bars represent averages over all relative velocities. Since we want the particles in our computational model to have the same λ (and ν) as real molecules, and the particle number density is reduced by a large factor, N, below the molecular gas density, the cross section of the computer particles in the computational model must be increased by the same factor of N.

It would be conceptually simple but computationally burdensome to keep track of the separations between all pairs of computer particles and simulate a collision whenever two particles come close together. This technique would require a large number of computational steps proportional to the square of the number of particles in order to check all possible collisions, which becomes extremely time consuming in large simulations. The alternative used by the Monte Carlo method preserves the average number of collisions per particle while performing a number of computational steps linearly proportional to particle number. In this method, we divide our computational volume into a large number of small spatial cells, each of which ideally should contain a fairly large number of particles. If the density and velocity field of the gas is nearly uniform throughout the cell, it is permissible to apply the mean collision rate deduced from Eq. (1) to all particles within the cell.

For every cell and time step in our computation, we randomly choose pairs of particles and decide whether they collide or not on the basis of their relative velocity, c_r. Their collision probability, $c_r \sigma_r(c_r)$, is divided by a maximum value $(c_r \sigma_r)_{\max}$, and the ratio is compared to a random number. If the random number is less than the ratio, we let the pair collide. When a pair of particles collides, a time counter for the cell is increased by an amount

$$\Delta\tau = 2V/(k^2 N c_r \sigma), \tag{2}$$

where V is the cell volume, k the number of particles in the cell, and N the number of molecules represented by each particle. (Note that Nk/V is the local gas density, n) More collisions are sought until the cell's time counter equals Δt, the duration of our computational time step. Thus the total number of collisions which have occurred in the cell during that time step is

$$N_{\text{coll}}(\Delta t) = \frac{\Delta t}{2} N k^2 \overline{c_r \sigma}/V = \frac{\Delta t}{2} k n \overline{c_r \sigma}. \tag{3}$$

Since each collision involves two particles, the average collision rate per particle is now in agreement with Eq. (1).

This Monte Carlo method is usually less time consuming than the deterministic method of seeking collisions, but it has disadvantages of its own. The random choice of particle pairs from a cell is based on assumed near-uniformity of the gas within the cell; this will require that a great number of cells be used when the mean density or velocity is expected to vary greatly throughout a computational volume (of course, this is also true for continuum fluid computations). Because it is desirable that particles not collide more than once per time step, our time steps ideally should be less than $1/v$, which may be quite small in some regions of a volume whose density is very nonuniform.

When two particles collide, their post-interaction velocities will depend on the interaction potential assumed and on their impact parameter (which may be randomly chosen). In the simulations described below, we have assumed hard-sphere scattering, which gives isotropic, elastic scattering of the particles' relative velocity vector and has a velocity-independent cross section, σ. More complicated potentials may be used, if desired, and the preceding formulae remain appropriate [3].

This Monte Carlo method must be refined in several ways for our simulations of a strongly stratified gas, principally because the gas density can vary over many orders of magnitude throughout the region of interest. It is possible to show, for example, for an isothermal gas inside a cylinder rotating with angular velocity Ω and a no-slip outer wall at radius R, that the phase-space particle density is proportional to

$$f(\mathbf{r}, \mathbf{v}) \propto \exp\left[\frac{-v_r^2-(v_\theta-r\Omega)^2-v_z^2+\Omega^2 r^2}{2v_d^2}\right], \tag{4}$$

where v_d is the one-dimensional velocity dispersion. (This formula may be derived by assuming that gas molecules are reflected/emitted inward from a rotating, cylindrical wall with a Maxwellian velocity distribution peaked at $\Omega R\hat{\theta}$; the velocity of a collisionless particle at any point in its trajectory can be determined from its velocity at the wall, and a coordinate transformation gives the distribution function, Eq. (4), in local coordinates.) Thus, we see that such "equilibrium" gas (i.e., the solution for no internal solid obstructions and uniform temperature $kT=mv_d^2$) is everywhere a Maxwellian with no z (i.e., axial) or θ dependence, mean velocity $r\Omega\hat{\theta}$, and radially varying density:

$$n(r)=n(R)\exp\left[\frac{\Omega^2(r^2-R^2)}{2v_d^2}\right]. \tag{5}$$

Note that the density can be normalized to some arbitrary reference radius r_0 rather than the wall simply by replacing R and $n(R)$ in Eq. (5) by r_0 and $n(r_0)$.

Since ΩR $(=v_{\text{wall}})$ is generally much greater than v_d for problems of practical interest, we expect the density to vary greatly throughout almost any computational volume we should wish to simulate. If we were to retain the same factor, N, for the number of molecules represented by a particle throughout our simulation region, we would have either an intractably large number of particles at large radii or a statistically small number at smaller radii. One solution [2] is to use different conversion factors at different radii, so that a particle at large r generally represents many more molecules than does a particle nearer the axis. Moreover, different cells may have different volumes, while we might want them all to contain approximately the same number of particles (which for computational efficiency, we want to be as small as can be consistent with reasonably good statistics). Bird [2] argues that this number of particles per cell may be allowed to become as small as 10 to 12. If we want to choose a conversion factor, N_i, which will give a constant number, k', of particles in each cell, i, for the ideal case of an unperturbed, isothermal stratified gas in "equilibrium," this factor is obtained from

$$N_i k'=\int_{\text{cell } i} n(r)\,d^3x=\left(\frac{v_d}{\Omega}\right)^2 \Delta\theta_i\,\Delta z_i\,n(r_0)$$
$$\times\left\{\exp\left[\frac{(r_{\max}^2-r_0^2)\,\Omega^2}{2v_d^2}\right]-\exp\left[\frac{(r_{\min}^2-r_0^2)\,\Omega^2}{2v_d^2}\right]\right\}, \tag{6}$$

where $\Delta\theta_i$ and Δz_i are the angular and axial widths of the cell, $r_{\max}$ and $r_{\min}$ are its outer and inner radial boundaries, and r_0 is a reference radius (fixed for all cells in a given simulation). For non-ideal cases of practical interest, where gas flow may be perturbed by internal obstacles, the conversion factors are still calculated from Eq. (6), and the ratio of a cell's actual particle number, k_i, to the ideal, k', equals the ratio of gas density to the idealized gas density specified by Eq. (5). The time counter $\Delta\tau_i$ in each cell i for every pair of particles undergoing a collision with relative velocity c_r is obtained from

$$(\Delta\tau_i)^{-1} = (\Delta t)^{-1} \int_{\text{cell}\, i} n_{\text{coll}}(\Delta t)\, d^3x = k_i \left(\frac{k_i}{k'}\right) \left(\frac{c_r}{4\sqrt{2}\,\lambda(r_0)}\right) \times \left\{ \exp\left[\frac{(r_{\max}^2 - r_0^2)\,\Omega^2}{2v_d^2}\right] + \exp\left[\frac{(r_{\min}^2 - r_0^2)\,\Omega^2}{2v_d^2}\right] \right\}, \tag{7}$$

where $n_{\text{coll}}(\Delta t)$ is the number of molecular collisions per unit volume in time Δt, and $\lambda(r_0)$ is the mean free path for the ideal case at the reference radius r_0.

This procedure becomes complicated when particles cross from one cell to another, if the new cell has a different factor N_j. Each particle from cell i, representing N_i molecules, must become N_i/N_j particles in cell j to represent the same number of molecules. If this ratio is less than unity, we randomly choose either to accept the particle unchanged or to annihilate it, with the acceptance probability equal to N_i/N_j. If this ratio is greater than unity, we duplicate the particle sufficient times to give mass conservation on the average. The duplicate particles are spread out along the trajectory which the original particle follows through the new cell. The velocity of each duplicated particle is the same as that of the original particle. (This duplication is not entirely equivalent to carrying the original particle into a new cell with its original weighting factor, N_i; the initially identical duplicate particles may become randomized, and thus nonidentical, due to collisions in the new cell.)

Hausman and Roberts [4] described a simplified DSMC model of stratified gas flow which used Cartesian coordinates and a quasi-gravitational force to mimic the centrifugal effects of a rotating gas. For the present work, we have developed a new computer code which utilizes cylindrical coordinates r, θ, and z (also see [5]). Our computational volume is divided into cells whose boundaries are surfaces of constant r, θ, and z. We have chosen to use the laboratory, non-rotating reference frame, so that no fictitious forces need to be added, and particles travel on straight-line trajectories between collisions. The solid obstructions which perturb the gas flow in our simulations are assumed to be stationary in the laboratory frame; if they rotated it would be necessary to choose a new computational frame of reference in which the obstacle is stationary, adding appropriate centrifugal and Coriolis forces to our treatment of the particles.

Hausman and Roberts [4] examined two different sets of boundary conditions, neither very realistic for describing a cyclindrical volume of rapidly rotating, strongly stratified gas. In one formulation, there was a solid, specularly reflecting boundary at the "bottom" of the computational volume (corresponding to large radii) and all other boundaries completely open, with new particles flowing in only through one face (the "upstream" boundary) and old particles flowing out of all faces except the bottom, as if these were vacuum boundaries. A second formulation made all faces reflecting walls, except the upstream and downstream faces, into and out of which, respectively, the particles flowed.

More realistic boundary conditions are used in the present simulations (also see [5]). Particles which are inside the computational volume are allowed to leave through any boundary. The distribution function, Eq. (4), can be used to calculate the expected inward flux of particles through any boundary, assuming the gas on the outside of the boundary is well approximated by an unperturbed, isothermal, rotational flow. We take the inward molecule flux at any location [2] to be

$$F = n(\mathbf{r})\, v_d[\exp(-s^2) + \sqrt{\pi}\, s(1 + \operatorname{erf}(s))]/\sqrt{2\pi}, \tag{8}$$

where

$$s \equiv \langle \mathbf{v}(\mathbf{r}) \rangle \cdot \hat{n}/(\sqrt{2}\, v_d), \tag{9}$$

and $\hat{n}$ is the inward unit normal vector of the surface. Since the mean velocity is in the $+\hat{\theta}$ direction, we have $s = 0$ for the z and r faces of our volume, and $s = \pm\Omega r/(\sqrt{2}\, v_d)$ for the upstream and downstream θ faces, respectively. The total molecular flux through the boundary of any finite-sized cell may be obtained by integrating Eq. (8) over the area of that boundary; application of the appropriate molecule-to-particle correction factor N_i [Eq. (6)] then tells how many particles we need to inject. Formulae derived for the determination of the number of particles required to be injected per unit time across each of the six boundaries of the computational volume are given in the Appendix.

The components of particle velocity parallel to a boundary are randomly chosen from Gaussians of standard deviation v_d and mean value $(0, r\Omega, 0)$; the distribution function of velocities normal to a boundary, however, is proportional to

$$f(v_n)\, dv_n \propto v_n \exp\left[-\left(\frac{v_n}{\sqrt{2}\, v_d} - s\right)^2\right] dv_n. \tag{10}$$

For r and z faces, as we have seen, s is zero, and Eq. (10) is easily invertible to give velocities from random numbers. For the upstream and downstream boundaries, however, s is given by Eq. (9), $s = \pm\Omega r/(\sqrt{2}\, v_d)$, and the velocities of input particles must be chosen by acceptance-rejection methods. Formulae derived for the determination of the velocity components and spatial locations for the injected particles across each of the boundaries are given in the Appendix.

The storage requirements of cells and particles make it impractical to model, for example, the full volume of a rapidly rotating, strongly stratified gas over a great many scale heights, and even modeling a full circumferential annulus generally requires some sacrifice in spatial resolution. However, some interesting situations are periodic in θ, as would occur if two, three, or more obstructions were all placed at the same radius and evenly spaced along a circumferential annulus. To accommodate these possibilities, the computational code is developed to provide the capability of simulating with higher resolution a fraction of a circumferential annulus, with periodic boundary conditions for the θ faces. Instead of putting new particles into the upstream face and letting old particles flow out the back, we may, if we choose, translate these outgoing particles back to the upstream face, giving them the same v_r, v_θ, v_z, r, and z values that they had as they left. The r and z boundaries are treated the same as they are for the nonperiodic assumption.

The addition of a solid obstacle to our simulation complicates the calculations in several ways. Most important, an obstacle will deflect any particle which strikes it. In order to find the intersection of a particle trajectory with a solid surface, we choose an obstacle whose surface can be described by quadric equations (in Cartesian coordinates) and utilize well-known formulae for the intersection point(s) of a straight line with a quadric surface. When a particle strikes the surface of an obstruction, it is diffusely scattered, with an emission velocity appropriate to the object's temperature. If the obstacle is concave in shape, it is possible for a reflected particle to strike it several times in one time step, so we check even the post-emission trajectory for further reflections.

Because the gas is likely to show structure on smaller scales near an obstacle than far away, the computational code is developed with the capability for specifying cells of different sizes in selected regions in order to put added resolution where it does the most good. This adds no new conceptual difficulties, as long as the various cell volumes are taken into account in our molecule-to-particle ratios [Eq. (6)] and our determinations of densities and collision rates [Eq. (7)].

III. RESULTS

Computational studies of the three-dimensional, hypersonic flow of stratified gas past an obstacle have been carried out, the gas stratified in a direction transverse to the incident mean flow. Different types and shapes of obstacles have been studied (e.g., a circular disk, a "long" solid rod, and a "short," cylindrical pipe with the downstream end covered by a flat plate containing an "orifice" of adjustable diameter). The Mach number of the incident gas has been varied in the range from 2 to 6, and different magnitudes of density stratification have been studied. In this paper we focus on several representative cases of the computed hypersonic flows, leaving other cases of interest to be discussed elsewhere. We limit our discusson herein to those computed hypersonic flows with an incident Mach number of $M = 4$ and to one type of obstructing object, namely the "short," cylindrical pipe with the downstream end covered by a flat plate containing an "orifice" of adjustable diameter. The computed results for hypersonic ($M = 4$) flows past the "short," cylindrical pipe are studied in cases for which the diameter of the "orifice" in the downstream endplate is varied.

Figure 1a shows a schematic of the cylindrical chamber adopted for our computational volume. The volume (which extends for half a circumference, $0 \leqslant \theta \leqslant \pi$) is divided by surfaces of constant r into 13 stratification layers; each layer is sub-

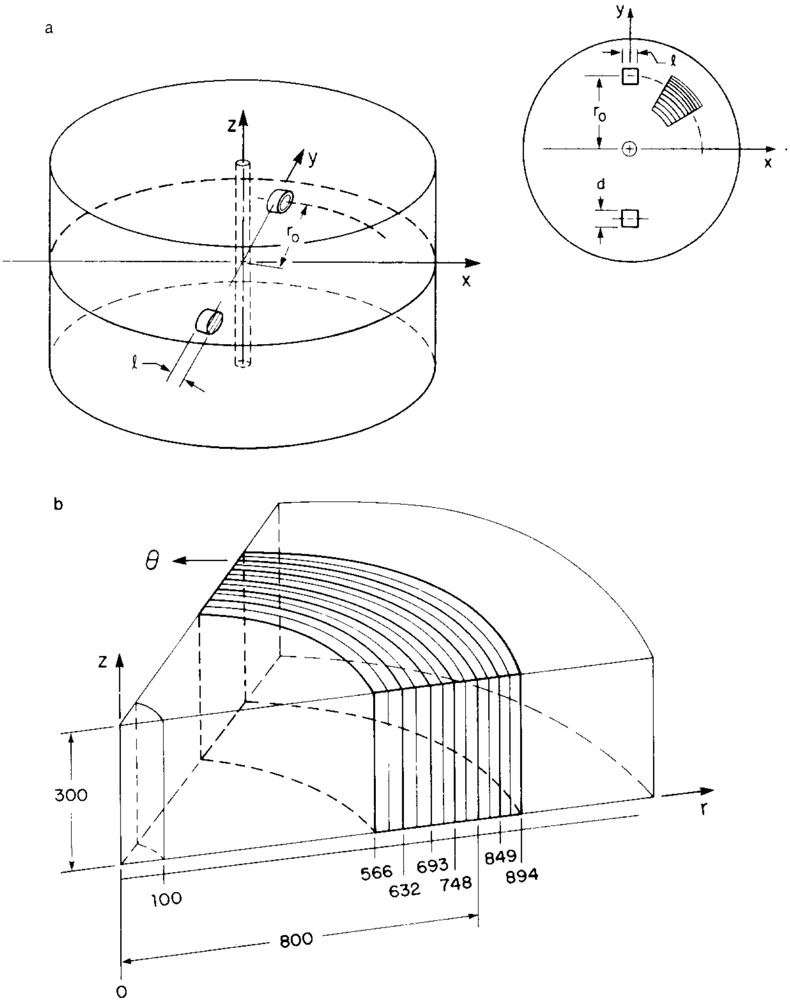

FIG. 1. Schematic of the computational chamber with the "short" obstructing cylindrical pipe. The pipe's open end faces into the flow; its downstream end is covered by a flat plate containing an "orifice" at its center which may be closed, partially open, or fully open. The pipe of length l ($= 100$ units) and outside diameter d ($= 100$ units) lies at a radial location r_0 ($= 800$ units) at which the unperturbed gas scale height H and mean free path λ are adopted as 50 and 20 units, respectively. A "mirror-image pipe" is also sketched at radial location r_0 but shifted about the chamber's central (z) axis in θ by π radians. (b) Representative sector-shaped, computational subvolume with selected r-stratification layers indicated.

divided by constant θ surfaces into "groups" (a total of 72); most groups are subdivided by constant z planes into "blocks" (a total of 116). The blocks are divided evenly in z and θ to give a total of 3000 cells; all of the cells within a single block are the same size. Figure 1b illustrates a representative sector-shaped subvolume of the computational chamber, with divisions labeled for selected stratification r-layers. Because the significant physical lengths are determined by scale heights and mean free paths, and velocity in terms of gas sound speed, all of which may vary in actual physical problems, we choose arbitrary units for both size and speed, and hence, time. The obstacle is a "short" cylindrical pipe of outer diameter $d = 100$ units, inner diameter 99 units, and length $l = 100$ units, centered on the y-axis $(\theta = \pi/2)$ at a radial location $r_0 = 800$ units from the central (z) axis of the chamber (Fig. 1a). The pipe faces into the flow with its upstream end fully open; its downstream end is covered by a flat plate containing an orifice at its center, which may be closed, partially open, or fully open. The radial location r_0 $(= 800$ units) from the chamber's central (z) axis to the pipe's center is adopted as the reference radius, at which the scale height H and mean free path λ of the (unperturbed) gas are chosen to be 50 and 20 units, respectively. For comparison, the size of the smallest (highest-resolution) cells in the computational volume is $25 \times 25 \times 12.5$ $(r \times \theta \times z$, units$^3)$. Periodic boundary conditions are adopted in θ to permit the simultaneous simulation of a "mirror-image pipe" shifted about the central axis in θ by π radians. The inner r boundary is an open surface (option 1, discussed in the Appendix) at a radius of 100 units from the central axis of the computational chamber (see Fig. 1b).

At the start of a simulation, computer particles, representing gas molecules, are distributed randomly in space within the computational volume. They are set in motion with a Gaussian velocity distribution, whose one-dimensional velocity dispersion v_d is 5 units, superposed upon a circular velocity corresponding to uniform, solid-body rotation with angular velocity 0.025 (inverse time) units. This gives a reference velocity, v_0, of 20 units (Mach number $M = 4$) at the reference radius, r_0, of 800 units. The uniform cylindrical pipe is taken to be a diffuse elastic scatterer, with emission velocities randomly chosen from Gaussians of standard deviation $v_d = 5$ units.

We will present computational results for hypersonic $(M = 4)$, stratified gas flow past the "short" cylindrical pipe in two limiting cases: first, case (1) in which the orifice in the pipe's downstream endplate is completely closed, and second, case (2) in which the orifice is fully open. Computations have also been carried out for hypersonic flow past the "short," cylindrical pipe in corresponding cases for which the gas is "unstratified." In these cases, the three-dimensional flow is directed down a rectilinear tube past the obstructing pipe, instead of being confined within a cylindrical computational chamber. These cases of "unstratified" gas flow provide the "standard" of comparison with respect to which cases (1) and (2) for stratified gas flow can be studied and compared. In the present paper we utilize the first of these "unstratified" cases as our representative "standard," denoted herein as case (3), namely that for hypersonic, "unstratified" flow past the "short," cylindrical pipe with the orifice in the downstream endplate completely closed. Comparisons of the stratified flow in case (1) with the unstratified flow in "standard" case (3) help to isolate important effects resulting from the density stratification of the gas (Section IV).

A. *Hypersonic* ($M = 4$), *Stratified Flow Past the "Short," Cylindrical Pipe: "Completely Closed" Orifice in the Downstream Endplate* (*Case* 1)

The effect of the obstructing pipe on hypersonically impinging, stratified molecular gas are studied first in the case for which the "orifice" in its downstream endplate is completely closed. It is useful to view the resulting three-dimensional density distribution and flow field from several different vantage points. Figure 2a shows a "side-view," z-θ projection of the density distribution of the molecular gas that lies within the cellular layer centered at mean radius $\bar{r} = 761$ units. This cellular layer has a thickness of 27 units, extending from $r = 748$ to $r = 775$ units and constitutes the innermost stratification layer of the five layers that cut through the volume of the pipe ($750 < r < 850$). The dark solid (straight) lines and the first and third tick marks on each of the four axes indicate the location of the minimum and maximum boundaries of the volume occupied by the pipe (both the length and outer diameter of the pipe equal 100 units). The middle tick mark on each of the axes indicates the location of the center of the pipe (on the θ-axis at $\theta = \pi/2$; on the z-axis at $z = 0$). Isodensity contours mark constant levels of molecular gas density. Labels on the contours denote the logarithm to the base ten of the number density $\log_{10}(n/n_c)$, after reduction by the same (large) scaling factor n_c throughout. Isodensity contours are separated by 0.075 increments of $\log_{10}(n/n_c)$. In this projection (viewing in a direction perpendicular to both the axis of the pipe and the central (z) axis of the computational chamber), strong "pile up" of the molecular gas is evident with considerable density enhancement within the pipe ($1.51 < \theta < 1.63$) and directly upstream of it ($1.40 < \theta < 1.51$), as indicated by the contour levels of $\log_{10}(n/n_c) = 5.25$ and higher. The maximum molecular gas density, $\log_{10}(n_{\max}/n_c) = 6.54$, occurs inside the pipe. Directly downstream ($\theta > 1.63$), the molecular gas system is strongly rarefied; note the contours levels lower than $\log_{10}(n/n_c) = 5.25$. In this region within one-half pipe length downstream of the back endplate, the molecular gas undergoes its minimum density, $\log_{10}(n_{\min}/n_c) = 4.94$. The pipe acts as a strong obstruction to the flow; the strong density variation in the molecular gas induced by the pipe spans a range of more than an order of magnitude between that in the compressed region upstream and within the pipe and that in the rarefied region downstream of the pipe. In fact, the computed density contrast $n_{\max}/n_{\min}$ ($10^{(6.54-4.94)} = 10^{1.60}$) is 39.8. Via representative $z - \theta$ projections such as this, we can see the reflection symmetry across the constant $z = 0$ midplane which contains the obstructing pipe's central axis (middle tick mark on the z axis).

Here we re-emphasize the distinction between "computer particles" and "molecular gas particles," each of the former representing N_i of the latter in a given cell$_i$, the latter constituting the real molecular gas system which is strongly stratified

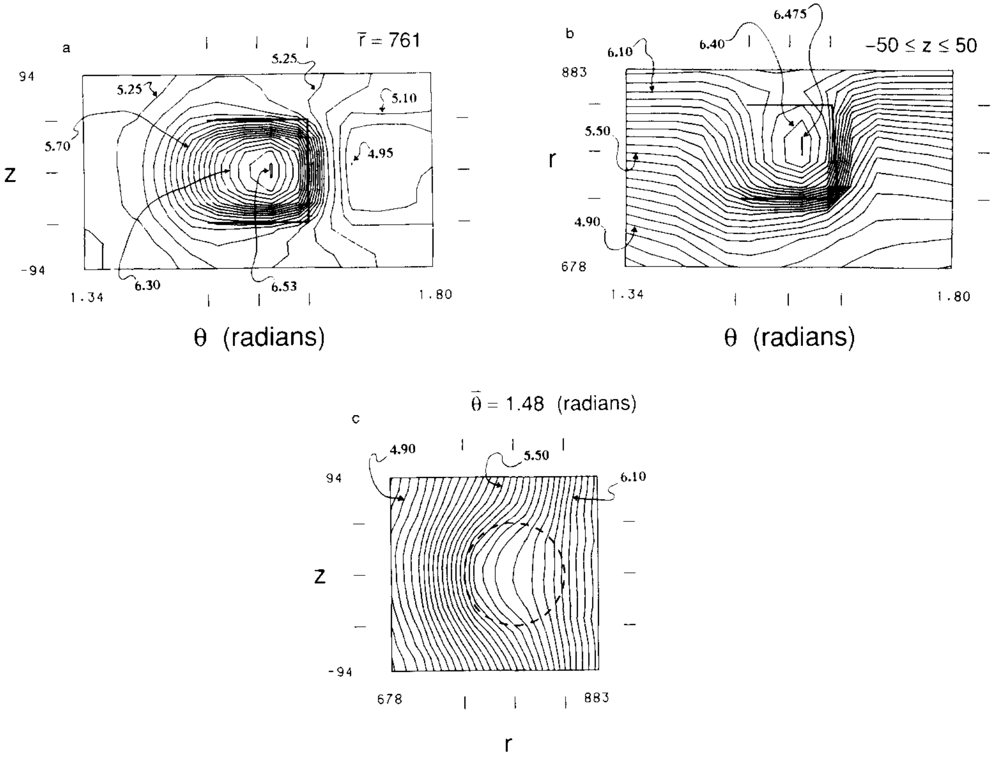

FIG. 2. Contours of equal "molecule" density resulting from the hypersonic flow of stratified gas (case 1) past the obstructing pipe with the "orifice" in the downstream endplate completely closed. (a) Isodensity contours in a representative z-θ projection containing the cellular r-stratification layer centered at average radius $\bar{r} = 761$. (b) Isodensity contours in a representative r-θ projection containing the computational slice, $-50 \leqslant z \leqslant 50$, centered on the pipe. (c) Isodensity contours in a representative z-r projection containing the computational slice centered at $\bar{\theta} = 1.48$ just in front of the pipe. Three tick marks on each of the four axes in these and subsequent contour maps indicate the location of the center of the pipe (middle tick mark) and the maximum and minimum values of the coordinates containing the volume occupied by the pipe. Density perturbations are prominent in the obstructed molecular gas in the neighborhood of the pipe and within it (Figs. 2a and 2b). Strong "r-asymmetry" in the resultant molecular gas density distribution is evident in the (radial) direction of the gradient of density stratification (Figs. 2b and 2c).

in the r direction. This is illustrated in Fig. 2b; shown is the density distribution of the "stratified molecular gas" in an $r-\theta$ projection of the computational volume, viewed from the vantage point of a "top-view" perspective. Sketched are isodensity contours for the molecular gas that lies between z-heights of -50 and 50 units. This $r-\theta$ computational slice contains the pipe. The pipe has a fixed length of 100 units (the θ-extent of this fixed length [in radians] is a smaller θ-projection at larger radii [$r = 850$ versus $r = 750$]). Note the systematic distortion of all isodensity contours in the vicinity of the pipe. Without the pipe to obstruct the flow, such isodensity contours, representing the radial stratification of a uniformly rotating (unperturbed) molecular gas, would appear as horizontal contours in this $r-\theta$ projection. Near the pipe, we see that high density contours are drawn inward just upstream, while low density contours are drawn outward just downstream, of the pipe. This systematic distortion underlines the strong density compression induced within and just upstream of the pipe and the strong rarefaction of the molecular gas just downstream. At smaller radii directly inward of the pipe, the density compression of the molecular gas is not as pronounced, but the enhancement is still detectable as far inward as the inner border at $r=678$. Note especially that inside the pipe where the compression of molecular gas is of greatest strength, there is virtually no radial stratification of the gas; collisions with the cylindrical side wall and the flat back wall (endplate with orifice closed [case 1]) have truncated virtually all of the gas's rotational motion within the pipe and thus removed the radial dependence of its

The distortion of the radial density stratification of the molecular gas system by the obstructing pipe can be viewed in detail through yet a third perspective. Figure 2c shows a $z-r$ projection of the molecular gas density distribution in a slice of computational volume with θ thickness of 0.035 radians, centered on $\bar{\theta}=1.48$ radians, just upstream of the leading edge of the pipe (1.51 radians $\leqslant \theta \leqslant 1.63$ radians). The dark, dashed circle delineates the actual circumference of the pipe; it is drawn as a "dashed" boundary to emphasize that the pipe lies entirely behind this slice of computational volume (this computational slice does not cut or touch the pipe). In this z-r projection of the region just upstream of the pipe, we can see clearly the systematic inward protrusion of isodensity contours. Without the pipe to obstruct the flow, such isodensity contours representing the r-stratification of a uniformly rotating (unperturbed) molecular gas would appear as vertical contours in this z-r projection. The strongest enhancement of molecular gas density occurs where the inward protrusion of isodensity contours is largest, namely near the $z=0$ midplane containing the central axis of the pipe. Note that the density enhancement shows reflection symmetry about the $z=0$ midplane. Although most pronounced directly in front of the pipe at radii slightly less than the radial location of the pipe's central axis, the enhancement of molecular gas density is evident at radii well inward of the pipe, in fact extending all the way to the inner border at $r=678$.

We now focus in greater detail on the strong compression and subsequent strong decompression of the gas and its distribution in the r, θ, and z directions. Figure 3a shows the variation, with respect to θ, of the number density of molecular gas $\log_{10}[n/n_c]$) at each of 10 different z-levels, all centered at the same representative average radius $\bar{r}=761$. The three tick marks on the horizontal axis denote the θ-extent of the pipe which is centered at the middle tick mark ($\theta=1.57$). The density peak and trough of molecular gas at each z-level delineates the strong gas compression within and just upstream of the pipe (the pronounced "mountain" in the contour map of Fig. 2a) as well as the gas decompression just downstream of the pipe (the broad "valley" in the contour map of Fig. 2a). The strongest compression

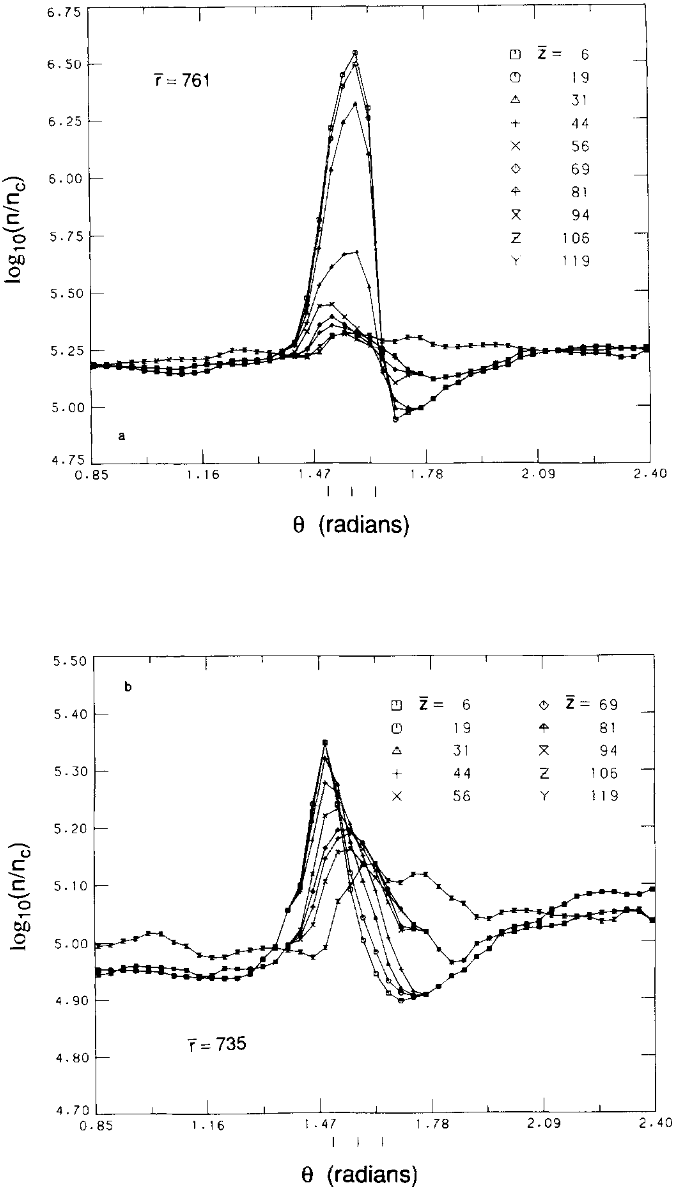

FIG. 3. Variation, with respect to θ, of the number density (plotted as $\log_{10}[n/n_c]$ on the vertical axis) of the stratified molecular gas (case 1), at each of 10 different z-levels, all centered at the same representative average radius: $\bar{r} = 761$ (a) and $\bar{r} = 735$ (b). The strong compression, as well as the subsequent strong decompression, occurs over a distance of several mean free paths of the perturbed molecular gas, both within the representative r-stratification layer cutting the volume of the pipe (a) and within the next inward r-stratification layer (just inward of the pipe) that does not cut or touch the pipe (b).

and strongest decompression are found within those z-levels which most fully intersect the volume of the pipe ($\bar{z}=6$ and 19). The enhancement in gas density to its maximum value ($\log_{10}[n_{\max}/n_c]=6.54$) takes place rapidly, with the sharpest rise occurring near the pipe's upstream end (marked by the first tick mark at $\bar{\theta}=1.51$). The location of sharpest decline coincides with the pipe's back wall (endplate with closed orifice, marked by the third tick mark [$\bar{\theta}=1.63$]), with the density minimum ($\log_{10}[n_{\min}/n_c]=4.94$) occurring just downstream [at $\theta=1.69$]). These strong density variations ($n_{\max}/n_{\min}=39.8$) induced in the molecular gas by the pipe subside rapidly thereafter in the downstream direction, with the gas relaxing rather quickly to a density near its equilibrium density ($\log_{10}[n_{\text{equil}}/n_c]=5.20$) within a distance less than four pipe lengths ($\theta<2.11$) downstream of the pipe's endplate.

At higher z-levels above the pipe (e.g., $\bar{z}=56$, 69, 81, 94, 106, and 119 in Fig. 3a), the density variations induced in the molecular gas by the pipe are much less strong. For example, even in the first z-levels just above the pipe at $\bar{z}=56$, the maximum density compression is only modest ($\log_{10}[n_{\max}/n_c]=5.44$); likewise modest is the density contrast $n_{\max}/n_{\min}(10^{(5.44-5.10)}=10^{0.34})$ of 2.19. These values for maximum density compression and density contrast are smaller than those at z-height $\bar{z}=6$ by factors of 12.6 and 18.2, respectively.

The distribution of molecular gas in the next inward r-stratification layer, centered at $\bar{r}=735$ is shown in Fig. 3b. This r-stratification layer is the closest layer to the pipe (inward of the pipe) that does not cut or touch the pipe. Plotted versus θ is the density distribution ($\log_{10}[n/n_c]$) of molecular gas in this layer, at the same 10 representative z-levels as in Fig. 3a. We first focus on the lowest z-levels. Most notable is the rapid rise in gas density, particularly at the two lowest z-levels ($\bar{z}=6$ and 19), which culminates in the sharp density peak ($\log_{10}(n_{\max}/n_c)=5.35$) near $\bar{\theta}=1.48$. The major proportion (90%) of this rapid density rise occurs over a distance of approximately one pipe length (100 units, $\bar{\theta}=1.34$ to $\bar{\theta}=1.48$), corresponding to several mean free paths of the perturbed molecular gas. We note that the mean free path λ of the perturbed gas in this region of rapid compression varies between its unperturbed value, $\lambda_{\text{unperturbed}}=69.8$ units, calculated from

$$\lambda(r)=\lambda(r_0)\exp\left[\frac{-\Omega^2(r^2-r_0^2)}{2v_d^2}\right], \tag{11}$$

where $r=735$, $r_0=800$, and $\lambda(r_0)=20$ units, on the one hand, and its minimum value $\lambda_{\min}=(\lambda_{\text{unperturbed}}n_{\text{unperturbed}}/n_{\max})=27.8$ units on the other. We thus recognize this region of rapid density rise as a shock wave in the molecular gas, whose thickness is no more than several collisional mean free paths.

Directly downstream of the pipe the molecular gas undergoes decompression, with the decrease from maximum density to unperturbed density occurring over a distance of about one pipe length (100 units, $\bar{\theta}=1.48$ to $\bar{\theta}=1.62$). What follows is a broad trough in the molecular gas distribution extending over a distance of approximately 180 units, slightly less than two pipe lengths ($\bar{\theta}=1.62$ to $\bar{\theta}=1.87$).

The average collisional mean free path of the decompressed gas in this broad trough ($\log_{10}(n_{\min}/n_c) = 4.90$) varies over a range between its unperturbed value, $\lambda_{\text{unperturbed}} = 69.8$ units, and its maximum value $\lambda_{\max} = (\lambda_{\text{unperturbed}} n_{\text{unperturbed}}/n_{\min}) = 78.4$ units. This broad trough of decompressed molecular gas therefore extends over a distance corresponding to no more than several collisional mean free paths in this low density region. From postshock peak density to minimum density in the broad trough, the molecular gas exhibits a total density contrast $n_{\max}/n_{\min}(10^{5.35}/10^{4.90} = 10^{0.45})$ of 2.82.

At higher and higher z-levels, it is evident in Fig. 3b that the density peak of molecular gas occurs further and further downstream. The extent of this downstream shift of the molecular gas density peak toward higher z can be more clearly appreciated through the perspective of a molecular gas density contour map. Displayed in Fig. 4a is one such representative contour map: a z-θ projection of the molecular gas density distribution in the r-stratification layer at average radius $\bar{r} = 735$. Only 15 isodensity contours that delineate the region of moderate to strong density enhancement are plotted. The strongest molecular gas compression lies along a "bow shock" which is parabolic-like in shape; it bends in the downstream direction from its broad base just upstream of the pipe's front end. At z-levels well above (and well below) the pipe near the upper (and lower) boundaries at $z = +94$ (and -94) (in Fig. 4a), the oblique bow shock and "density compression ridge" make an angle of approximately 30° (and −30°) with respect to the θ-direction, respectively.

Figures 4b and 4c display z-θ projections of the v_z component of velocity and the v_r component of velocity, respectively, in this same r-stratification layer at $\bar{r} = 735$. The v_z velocity component (Fig. 4b) attains its maximum value ($v_{z_{\max}} = +3.25$) at a location along the oblique density ridge (in Fig. 4a) above the pipe and its minimum value ($v_{z_{\min}} = -3.25$) along the oblique density ridge (in Fig. 4a) below the pipe. The thickness of this shock region over which the strongest density and v_z velocity gradients are induced is of the order of a pipe length, which corresponds to several mean free paths of the molecular gas ($27.8 < \lambda < 69.8$) in this region.

The isovelocity contours for the v_r component of velocity (Fig. 4c) show that the entire v_r field is negative and thereby directed inward in the (radial) direction of gradient of density stratification. A strong radial inflow of molecular gas, induced by the pipe, is evident in this r-stratification layer just inward of the pipe (in Fig. 4c). The most negative v_r values lie along a "valley" which is parabolic-like in shape and closely aligned with the density ridge of compressed molecular gas (in Fig. 4a). The parabolic-shaped v_r valley exhibits negative v_r values (-3.25 to -5.50) whose magnitudes are greater than those attained by v_z ($v_{z_{\max}} = 3.25$, $v_{z_{\min}} = -3.25$, in Fig. 4b). The most negative v_r value (-5.50) is attained at $\bar{\theta} = 1.48$, just upstream of the front end of the pipe.

Figure 4d displays an $r - \theta$ projection of the v_r velocity component for molecular gas that lies between the z-heights of -50 and 50 units. In this perspective, the magnitude and extent of the radial inflow induced by the pipe can be examined more fully. We see that the radial inflow is indeed strong in front of and inward of

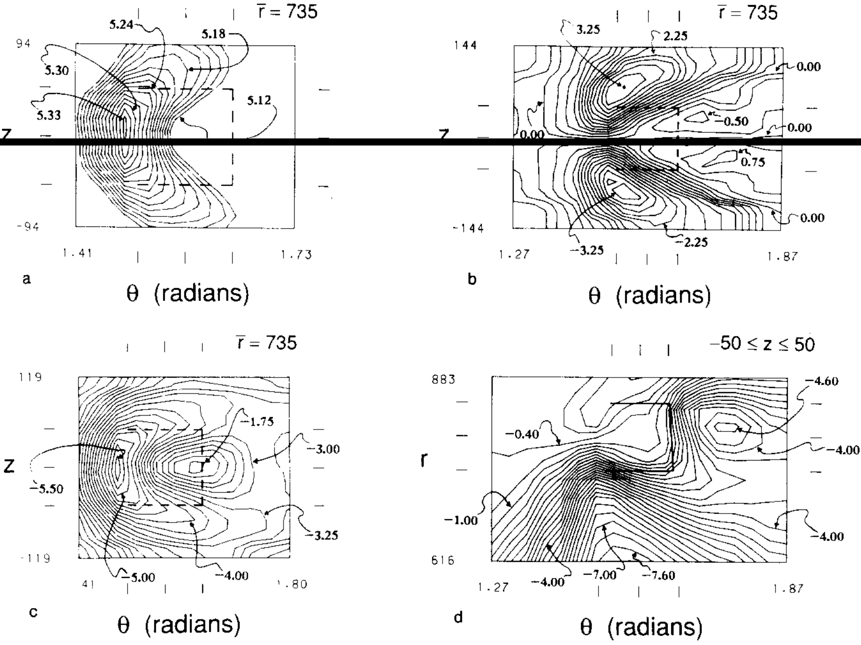

FIG. 4. (a) Contours of equal "molecule" density for the hypersonic, stratified flow (case 1) in a z-θ projection containing the cellular r-stratification layer at average radius $\bar{r} = 735$. The strongest molecular gas compression lies along a "bow shock" which is parabolic-like in shape in this projection. (b) Isovelocity contours of the v_z velocity component for the molecular gas (case 1) in the same r-stratification layer at $\bar{r} = 735$. (c) Isovelocity contours of the v_r velocity component for the molecular gas (case 1) in the same r-stratification layer at $\bar{r} = 735$. (d) Isovelocity contours of the v_r velocity component for the molecular gas (case 1) in the r-θ projected computational slice, $-50 \leqslant z \leqslant 50$, containing the pipe. The bow shock passing through a region has a thickness of several collisional mean free paths of the stratified molecular gas in that region. The broadening of the v_r minimum with decreasing radial position (d) is primarily a result of the increasing collisional mean free path in that direction of the gradient of density stratification.

the pipe, as was discovered in Fig. 4c. Note, however, that the radial inflow becomes even stronger at smaller radial distances. The most negative values attained by the v_r velocity component occur along a "valley" that extends inward in radius from the front end of the pipe. This "v_r" valley becomes deeper with decreasing radial position; values for v_r dip as low as -7.6 to -7.9 within the lowest contour level near the inner boundary ($\bar{r} = 616$).

The v_r valley characterizing the minimum in the v_r velocity component broadens in its θ extent with decreasing radial position all the way inward to the inner boundary (and beyond). This broadening is largely a result of the increasing collisional mean free path λ of the stratified molecular gas with decreasing radial position. The obstructed gas's mean free path increases globally in the inward radial direction much like that of unperturbed gas (when no obstacle is present) and also undergoes local variations which are strongest in the neighborhood of the pipe and within it. We note that the mean free path appropriate for unperturbed gas in the

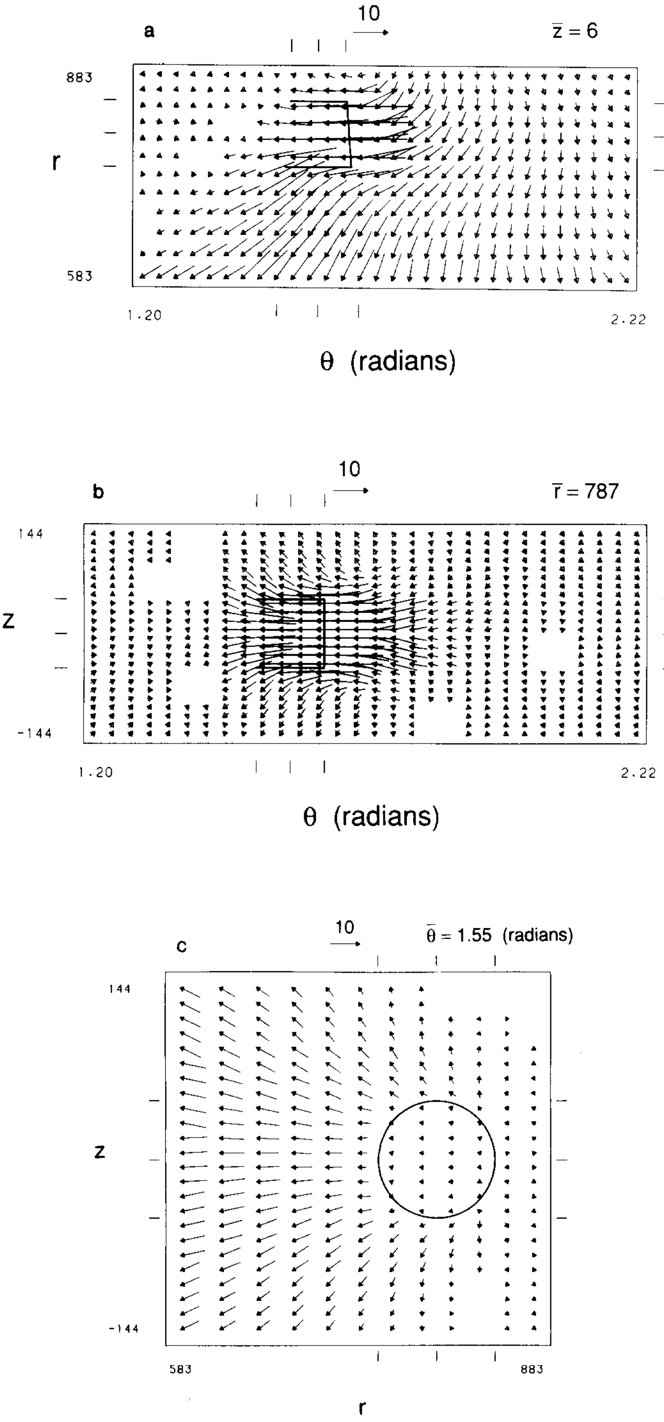
a
10
z̄ = 6
883
r
583
1.20
2.22
θ (radians)
b
10
r̄ = 787
144
z
-144
1.20
2.22
θ (radians)
c
10
θ̄ = 1.55 (radians)
144
z
-144
583
883
r

r-stratification layer at the inner boundary is $\lambda_{\text{unperturbed}} = 516$ units [calculated from Eq. (11)]. This unperturbed value (at $\bar{r} = 616$ units) is greater by a factor of 25.8 than that corresponding value for unperturbed gas, $\lambda_{\text{unperturbed}} = 20$ units, at the reference radius r_0 ($= 800$ units). Note that only a small fraction of the apparent broadening is caused by the mapping of the (r-θ, cylindrical coordinate) computational volume onto the Cartesian grid in the display presented (Fig. 4d). Such a mapping naturally entails a slight stretching of the θ-scale at smaller radii and a slight shrinking of the θ-scale at larger radii (e.g., as evidenced by the difference in spacing between the two sets of three tick marks along the horizontal axes, each delineating the same fixed pipe length [of 100 units]). Thus the predominant fraction of the broadening with decreasing radial position is attributed to the rapid increase in the collisional mean free path in that direction. Such broadening effects with decreasing radial position, and increasing collisional mean free path, are also manifested in the molecular gas density distribution. Indeed, the isodensity contour maps of Figs. 2b, 2c, and 8b show that the major enhancement in molecular gas density induced by the pipe broadens substantially near the inner boundary there (at $\bar{r} = 678$).

It is evident that the radial inflow induced in the molecular gas by the obstructing pipe is strong. We seek to gain further insight into this radially driven gas inflow and at the same time come to a deeper understanding of the overall dynamics of the stratified molecular gas as it impinges hypersonically on the obstructing pipe. To do so, we focus on the motion of the gas from the vantage point of an observer fixed in the rotating coordinate frame of solid body rotation for unperturbed gas (e.g., without the presence of an obstructing pipe). Such an observer, rotating about the central z-axis of the computational chamber at the angular speed of the unperturbed gas' solid body rotation, would measure the gas motion in terms of a velocity field of "reduced" vector velocities. Each "reduced" vector velocity would consist of the perturbed gas' total (inertial frame) vector velocity minus the circular velocity corresponding to solid body rotation at that radius. Figures 5a, 5b, and 5c provide three different projections of this "reduced" velocity field for gas near the obstructing pipe. Note the reference arrow, of magnitude 10 velocity units, at the top of Figs. 5a, 5b, and 5c. Arrows are plotted only for those cells whose total computed velocity is different from the "unperturbed" circular velocity by a significance level of more than two standard deviations. With respect to our observer's rotating reference frame, note that solid-body rotating unperturbed gas (without the presence of an obstructing pipe) would have

---

FIG. 5. Velocity field maps for the stratified molecular gas (case 1) in selected regions of the computational volume containing the "closed orifice" obstructing pipe, pictured with respect to an observer moving at the angular speed of the incident (solid body rotating) mean flow. (a) A representative r-θ projection of the computational slice centered at average z-height $\bar{z} = 6$. (b) A representative z-θ projection of the cellular r-stratification layer centered at average radius $\bar{r} = 787$. (c) A representative z-r projection of the computational slice centered at $\bar{\theta} = 1.55$. Strong radially driven gas inflow (Figs. 5a and 5c) is a major "three-dimensional" characteristic of all the hypersonic, stratified flows studied when an obstructing object is present.

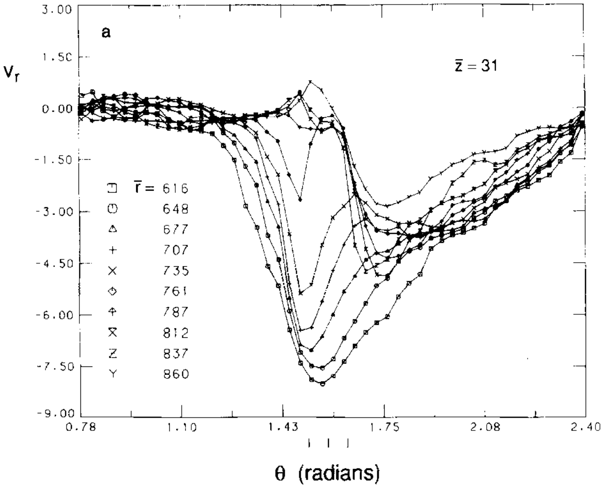
a
$\bar{z} = 31$
V_r
3.00
1.50
0.00
-1.50
-3.00
-4.50
-6.00
-7.50
-9.00
0.78
1.10
1.43
1.75
2.08
2.40
θ (radians)
□ $\bar{r}$ = 616
○ 648
△ 677
+ 707
× 735
◇ 761
787
812
Z 837
Y 860

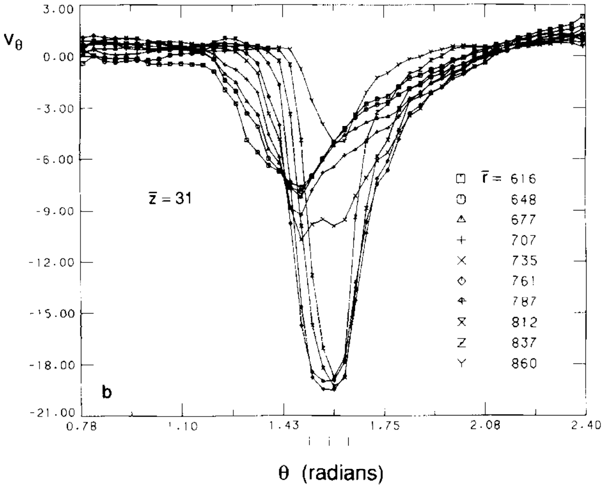
b
$\bar{z} = 31$
V_θ
3.00
0.00
-3.00
-6.00
-9.00
-12.00
-15.00
-18.00
-21.00
0.78
1.10
1.43
1.75
2.08
2.40
θ (radians)
□ $\bar{r}$ = 616
○ 648
△ 677
+ 707
× 735
◇ 761
787
812
Z 837
Y 860

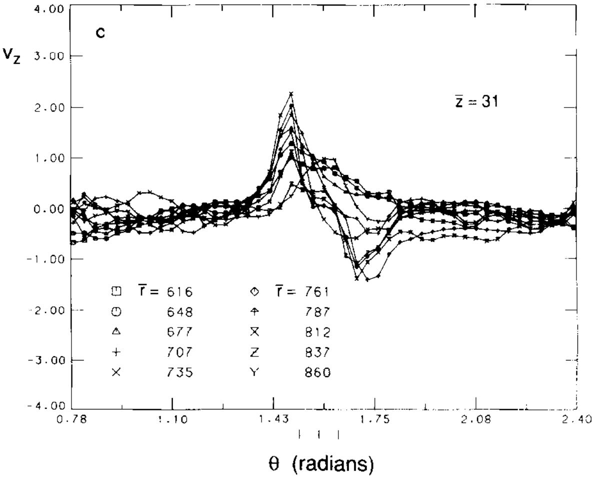
c
$\bar{z} = 31$
V_z
4.00
3.00
2.00
1.00
0.00
-1.00
-2.00
-3.00
-4.00
0.78
1.10
1.43
1.75
2.08
2.40
θ (radians)
□ $\bar{r}$ = 616
○ 648
△ 677
+ 707
× 735
◇ $\bar{r}$ = 761
787
812
Z 837
Y 860

zero velocity everywhere, and consequently its arrows would not be plotted. Figures 5a and 5b show that the flow is strongly decelerated by the pipe. Furthermore, we see more fully the extent of the strong radial inflow (Fig. 5a) induced by the pipe; its influence is not only partly upstream of the pipe but also well downstream and all the way inward to the inner boundary (at $\bar{r} = 583$) and beyond. The magnitude of this radial component of velocity, v_r, is indeed large relative to the z component of velocity, v_z (Fig. 5c). To be sure, the obstructing pipe induces strong systematic motions in the gas; the pipe not only retards the flow in passage of gas past the pipe but also strongly drives the obstructed gas radially inward over considerable distances.

The velocity perturbations induced in the gas by the obstructing pipe are shown in more detail in Figs. 6a, 6b, and 6c. We display, versus θ, the perturbed velocity components, v_r, v_θ, and v_z in 10 different r-layers, all at the average z-height $\bar{z} = 31$ (again v_θ is prescribed with respect to the observer rotating with the mean flow). The systematic depression of the v_θ velocity component of the perturbed flow (Fig. 6b) toward large negative values reflects the strong retardation of the flow by the pipe. The gas within r-stratification layers extending through the volume of the pipe ($\bar{r} = 761$, 787, 812, and 837), as expected, undergoes the most prominent retardation; minimum values for the perturbed v_θ component are in the range -19.0 to -20.0. A fraction of the gas in these r-layers becomes trapped inside the pipe. Gas at radial distances well interior ($\bar{r} = 616$, 648, 677, and 707) to the pipe's radial location, as well as exterior ($\bar{r} = 860$), also feels prominent retardation in its mean flow, with minimum values for the perturbed v_θ component of -6.0 to -9.0, even though the pipe itself does not penetrate these r-layers.

The large, broad depression in the v_r velocity component (Fig. 6a) illustrates the magnitude of the strong inward-driven flow induced by the obstructing pipe. Its magnitude is strongest for the innermost r-stratification layers at radii, $\bar{r} = 616$, 648, 677, and 707, well interior to the radial location of the pipe, with minimum v_r values in the range of -6.0 to -8.0. Note how far downstream the radially driven inflow persists, subsiding only by angular position 2.20 radians, corresponding to a linear scale of approximately four to five pipe lengths downstream from the center of the pipe. In contrast, the v_θ depression (Fig. 6b), comparable in magnitude for these innermost r-layers ($\bar{r} = 616$, 648, 677, and 707) and much larger in magnitude for the r-layers penetrating the volume of the pipe, extends to only about 1.85 radians, corresponding to a linear scale of approximately two pipe lengths downstream of the pipe's center.

This broad radial gas inflow (Fig. 6a) is now seen to account for the prominent protrusion of high-density gas inward of the pipe (Figs. 2b and 2c). This broad gas

FIG. 6. Variation, with respect to θ, of the v_r velocity component (a), the v_θ velocity component (b), and the v_z velocity component (c) for the stratified molecular gas (case 1) in 10 different r-stratification layers, all within the same computational slice at average z-height $\bar{z} = 31$ (midway between the pipe's central axis and the uppermost part of the pipe's cylindrical surface). The radially driven gas inflow is particularly prominent in the inner r-stratification layers (a).

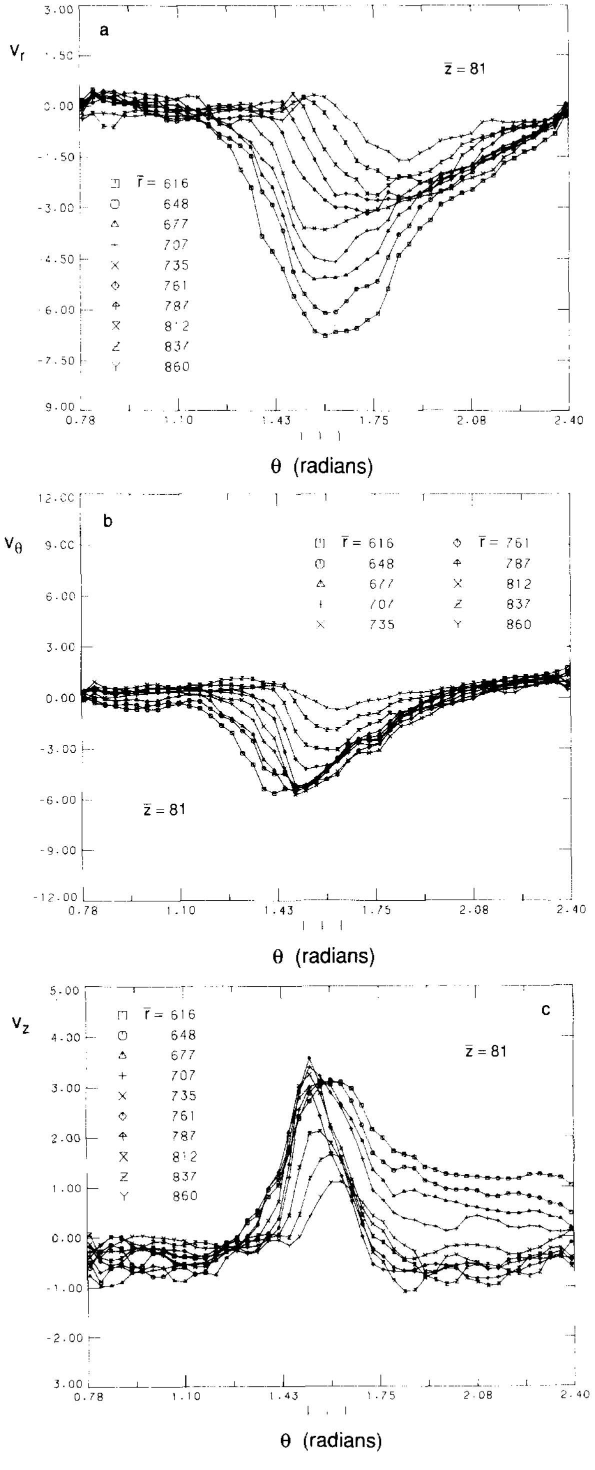
a
V_r
3.00
1.50
0.00
-1.50
-3.00
-4.50
-6.00
-7.50
-9.00
$\bar{z} = 81$
$\bar{r}$ = 616
648
677
707
735
761
787
812
837
860
0.78
1.10
1.43
1.75
2.08
2.40
θ (radians)
b
V_θ
12.00
9.00
6.00
3.00
0.00
-3.00
-6.00
-9.00
-12.00
$\bar{r}$ = 616
648
677
707
735
$\bar{r}$ = 761
787
812
837
860
$\bar{z} = 81$
0.78
1.10
1.43
1.75
2.08
2.40
θ (radians)
c
V_z
5.00
4.00
3.00
2.00
1.00
0.00
-1.00
-2.00
-3.00
$\bar{r}$ = 616
648
677
707
735
761
787
812
837
860
$\bar{z} = 81$
0.78
1.10
1.43
1.75
2.08
2.40
θ (radians)

density enhancement is a collisional effect, due to the scattering produced when the deflected flow interacts with the incoming flow. Note that the gas in r-layers penetrating the volume of the pipe ($\bar{r}=761$, 787, 812, and 837 in Fig. 6a) does not participate fully in this radial inflow until a θ location is reached just downstream of the pipe ($\theta > 1.63$). A fraction of the gas in these r-layers just upstream of $\theta = 1.63$ becomes trapped inside the pipe. Likewise, gas at radii greater than the radial location of the pipe ($\bar{r}=860$) participates in the radial inflow only downstream of the pipe, the minimum value of -3.0 for its perturbed v_r velocity component occurring in the θ range: $1.70 < \theta < 1.80$.

The increase of the v_z velocity component (Fig. 6c) to moderately positive values ($+2.0$) upstream of the pipe and its subsequent decrease to moderately negative values (-1.5) downstream ($\bar{r}=761$, 787, 812, and 837) illustrate the degree to which the molecular gas "spills over" the pipe in the z-direction. Note that gas in r-stratification layers at radii interior to the pipe's radial location ($\bar{r}=616$, 648, 677, 707, and 735) is perturbed similarly in the z-direction and also attains moderately positive perturbed v_z values, particularly gas at $\bar{r}=707$ and 735, even though the [illegible] gas at radii ($\bar{r}=860$) greater than the pipe's radial location is weakly perturbed similarly in the z-direction but shifted somewhat downstream.

The gas velocities at higher and lower z-levels are also intriguing. Figures 7a, 7b, and 7c show corresponding curves for the v_r, v_θ, and v_z velocity components in the same 10 representative r-layers but at average z-height $\bar{z}=81$, approximately 1.6 pipe radii (6 to 7 cell widths) above the central plane of the computational volume. The moderate depression in the v_θ component of velocity (Fig. 7b) shows that the mean flow at this z-height is retarded by the pipe, but less strongly than at z-heights closer to the central $z=0$ midplane of the computational volume. Gas in the innermost five (or six) r-stratification layers undergoes the strongest retardation at this z-height. Minimum values for the v_θ velocity component are in the range of -5.0 to -6.0 ($\bar{r}=616$, 648, 677, 707, and 735 in Fig. 7b), moderately reduced from the range of -6.0 to -9.0 exhibited by gas within the same r-layers at average z-height $\bar{z}=31$ (Fig. 6b). Note that gas within the outer r-stratification layer ($\bar{r}=860$, Fig. 7b) at this z-height $\bar{z}=81$ undergoes no significant retardation in its mean flow.

Most striking at this z-height is the strong radially driven gas inflow, reflected by the strong depression of the perturbed v_r velocity component (Fig. 7a), extending to considerable distances in the θ direction downstream of the pipe. The radial gas inflow is characterized by a behavior closely similar to that of gas nearer the $z=0$ midplane of the computational volume (e.g., $\bar{z}=31$, Fig. 6a). The distance in the θ-direction over which radial inflow persists at this z-height is also quite impressive,

---

FIG. 7. Variation, with respect to θ, of the v_r velocity component (a), the v_θ velocity component (b), and the v_z velocity component (c) for the stratified molecular gas (case 1) in the same 10 r-stratification layers as in Fig. 6, but here within the computational slice at average z-height $\bar{z}=81$ (approximately 1.6 characteristic pipe radii [six to seven cell widths] above the central axis of the pipe). The radially driven gas inflow is still prominent at this z-height well above the pipe.

as it was at lower z-heights (e.g., $\bar{z}=31$, Fig. 6a). Note that the minimum value for the v_r velocity component lies in the range -6.0 to -7.0 ($\bar{r}=616$ and 648), comparable with that of -6.0 to -8.0 found at z-height $\bar{z}=31$ (Fig. 6a).

The maximum value of approximately $+3.0$ achieved by the v_z velocity component (Fig. 7c) indicates the degree of upward expansion of perturbed gas at this z-height. Note that this upward expansion is most prominent, with largest magnitude and greatest extent downstream, for inner r-stratification layers well inward of (and well above) the pipe itself. Comparison of velocity magnitudes in Figs. 7a and 7c shows that the perturbed velocity of the gas in the inner r-layers at this z-height is directed more nearly in the inward ($-r$) and upward ($+z$) direction.

B. *Hypersonic* ($M=4$), *Stratified Flow Past the "Short," Cylindrical Pipe: "Fully Open" Orifice in the Downstream Endplate* (*Case* 2)

The effects of the obstructing pipe on hypersonically impinging, stratified molecular gas are now studied in the case for which the "orifice" in its downstream endplate is fully open. Again the pipe faces into the flow with its upstream end fully open. The "open orifice" in the downstream endplate is "one-sided" in the sense that gas passing down the pipe in the direction of the mean flow may enter the orifice but gas outside the pipe that impinges upon the downstream endplate from behind cannot enter the pipe through (the backside of) the orifice. We focus on the case of a "fully opened" orifice with diameter equal to the inner diameter of the pipe itself. In an effort to simulate the withdrawal of gas by a scoop, any computer particle (and gas molecule) that passes down the pipe and through the orifice is assumed to be lost from the computational chamber.

It is important to consider the stratification of the real molecular gas system and focus on similarities and differences that arise in the "closed orifice" and "open orifice" cases. Figures 8a and 8b show isodensity contours of the molecular gas for the "open orifice" simulation in the same $z-\theta$ and $r-\theta$ projections as shown for the "closed orifice" simulation in Figs. 2a and 2b. Labels on the contours again denote the logarithm to the base 10 of the number density, $\log_{10}(n/n_c)$, scaled by the same (large) constant scaling factor, n_c, as in the "closed orifice" case. Enhancements to high molecular gas density are strong within and upstream of the pipe, although the maximum density along the pipe's interior cylindrical surface is somewhat milder in the "open orifice" case (maximum contour level near 6.09 in Fig. 8a) than that in the "closed orifice" case (maximum contour level of 6.54 in Fig. 2a). The density depression behind the pipe is just slightly lower in the "open orifive" case (minimum near 4.90, Fig. 8a) than that in the "closed orifice" case (minimum of 4.94, Fig. 2a). Thus despite the fact that the "open orifice" case represents the extreme case of minimum impedance for the flow (maximum withdrawal of gas), the variation of molecular gas density between maximum and minimum values is still of a magnitude approximately 40% that between the corresponding maximum and minimum values for the "closed orifice" case. High density contours at high r-stratification layers (Fig. 8b) are strongly deflected

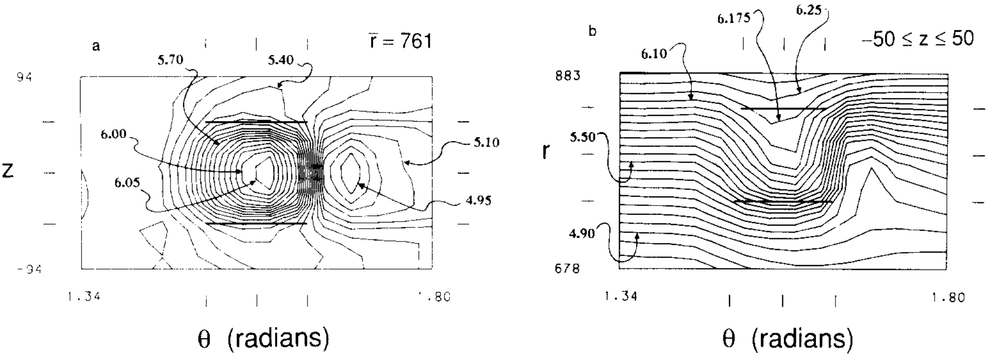

FIG. 8. Contours of equal "molecule" density for the hypersonic flow of stratified gas (case 2) past the obstructing pipe with the "orifice" in the downstream endplate fully open. (a) Isodensity contours in the same z-θ projected cellular r-stratification layer centered at average radius $\bar{r} = 761$, as in Fig. 2a. (b) Isodensity contours in the same r-θ projected computational slice, $-50 \leqslant z \leqslant 50$, containing the pipe, as in Fig. 2b. This case 2 represents the case of minimum impedance for the flow (maximum withdrawal of gas); yet the density perturbations are still prominent and are of a magnitude approximately 40% that in case 1 which represents the case of maximum impedance for the flow (no withdrawal of gas).

inward in radius by the influence of the obstructing pipe and replace lower density contours in the region within and upstream of the pipe, whether or not the orifice is completely closed (Fig. 2b), partially open, or fully open (Fig. 8b). Note, however, that gas inside the "open orifice" pipe retains much of its radial stratification (Fig. 8b) in contrast to that for gas in the "closed orifice" case (Fig. 2b).

In the "open orifice" case, prominent retardation of gas still occurs in r-layers cutting the volume of the pipe, with a depression in the perturbed v_θ velocity component to values of -13 to -16 ($\bar{r} = 761$, 787, 812, and 837). The magnitude of this v_θ perturbation is still 70% to 80% that found in the "closed orifice" case (minimum values for v_θ of -19 to -20, Fig. 6b). At r-layers both interior and exterior to the pipe, the v_θ component shows only a weak depression to values of -3.0 to -4.0, except for the $\bar{r} = 735$ layer just interior to the radial location of the pipe where the retardation of the gas is somewhat stronger (v_θ depression to values near -6.0).

Figures 9a, 9b, and 9c display the variations, with respect to θ, of the v_r velocity component at average z-height $\bar{z} = 31$, the v_r velocity component at average z-height $\bar{z} = 81$, and the v_z velocity component at average z-height $\bar{z} = 81$, respectively, for gas in the same 10 representative r-stratification layers as shown for the "closed orifice" case in Figs. 6a, 7a, and 7c. Most notably, the radially driven inflow induced in the gas by the obstructing pipe is prominent in all 10 r-stratification layers (Fig. 9a), just as in the "closed orifice" case (Fig. 6a). Both the magnitude of the depression in v_r velocity component and the broad θ-extent of the v_r depression, over which the effect of radial inflow is significant, do not change greatly with z-height (e.g., $\bar{z} = 31$ [Fig. 9a] vs $\bar{z} = 81$ [Fig. 9b]), much like the v_r depression in the "closed orifice" case (e.g., $\bar{z} = 31$ [Fig. 6a] vs $\bar{z} = 81$ [Fig. 7a]). A large v_r

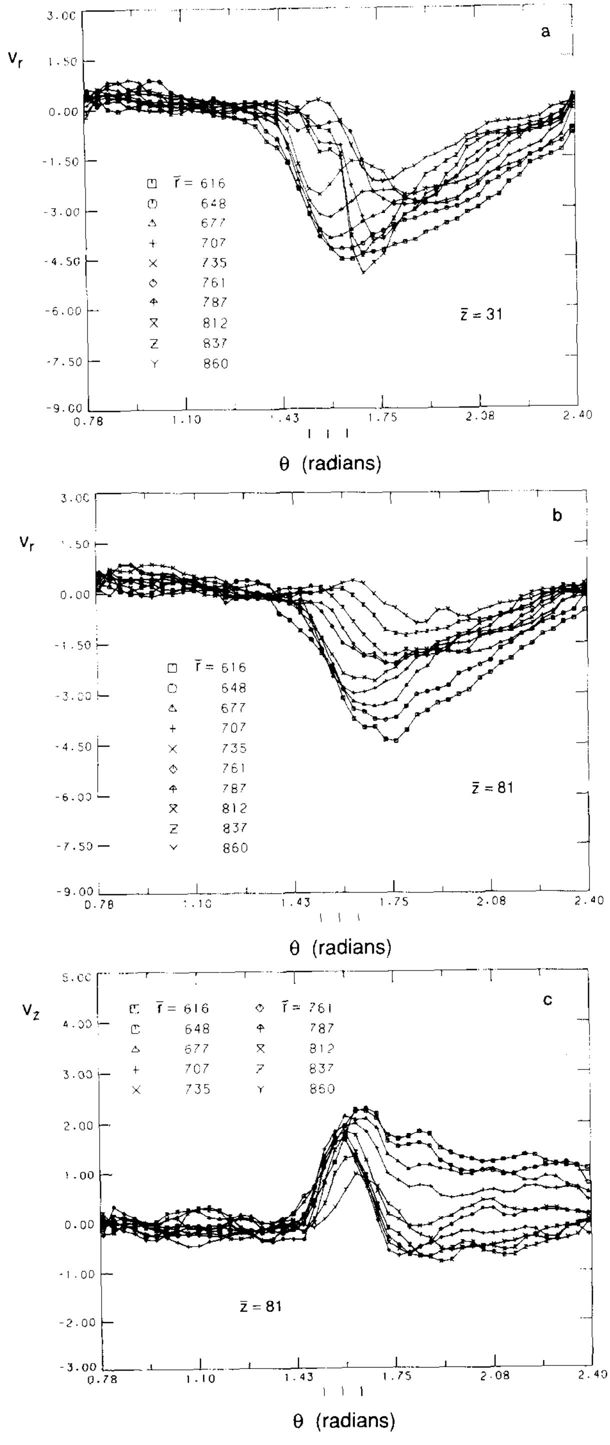
a
V_r
3.00
1.50
0.00
-1.50
-3.00
-4.50
-6.00
-7.50
-9.00
0.78
1.10
1.43
1.75
2.08
2.40
$\bar{r}$ = 616
648
677
707
735
761
787
812
837
860
$\bar{z}$ = 31
θ (radians)
b
V_r
$\bar{r}$ = 616
648
677
707
735
761
787
812
837
860
$\bar{z}$ = 81
θ (radians)
c
V_z
5.00
4.00
3.00
2.00
1.00
0.00
-1.00
-2.00
-3.00
$\bar{r}$ = 616
648
677
707
735
$\bar{r}$ = 761
787
812
837
860
$\bar{z}$ = 81
θ (radians)

depression (minimum of -4.5 [Fig. 9a]) still occurs in those r-stratification layers at radii interior to the pipe's radial location. This large v_r depression has a magnitude of approximately 60% that in the "closed orifice" case (minimum v_r of -7.5, Fig. 6a). The broad θ-extent of the v_r depression is still much greater than the θ-extent of the v_θ depression, the latter representing the region over which retardation of the mean gas flow by the obstructing pipe is strong.

[redacted] somewhat from that experienced for the "closed orifice" obstructing pipe. Here the v_z velocity component at z-height $\bar{z} = 81$ exhibits a positive peak of magnitude approximately 2.0 in the region just above the obstructing pipe and at radii interior to its radial location. This v_z peak is approximately two-thirds the magnitude of the v_z peak of 3.0 at the same z-height $\bar{z} = 81$ in the "closed orifice" case (Fig. 7c). With the orifice in the downstream endplate fully open allowing substantial gas withdrawal, there is a much lower pressure maximum within and just upstream of the pipe, resulting in much less splattering of gas upward (and downward) in the z direction in the region directly upstream of the pipe and at z-heights above (and below) the pipe. Thus for the "open orifice" case, there is less gas spilling over (and under) the pipe at positive (and negative) z-heights.

In the region just downstream of the pipe at z-height $\bar{z} = 31$, the v_z component of velocity sharply decreases through negative values, reaching a minimum of approximately -3.0. The resulting v_z downflow is of a magnitude approximately double that for the "closed orifice" case (minimum value -1.5 in Fig. 6c). This stronger negative v_z downflow of gas from positive z-heights (as well as stronger positive v_z upflow from negative z-heights) in the "open orifice" case is indicative of the more substantial gas replenishment taking place in the low-pressure region just downstream of the pipe, itself a consequence of the substantial gas withdrawal through the pipe's fully open ("one-sided") orifice.

IV. Conclusions and Discussion

The computational simulations we have carried out, modeling the hypersonic interaction of a rarefied, stratified gas with an obstacle comparable in size to the gas scale height and mean free path, show several common major characteristics despite differences in Mach number, gas density scale height, and shape of obstructing object. First and foremost is the strong and extensive net inward motion induced in the scattered gas (Figs. 4c, 4d, 5a, 5c, 6a, 7a, 9a, and 9b). This radial inflow, prominent not only in the neighborhood of the obstacle and

FIG. 9. Variation, with respect to θ, of the v_r velocity component at z-height $\bar{z} = 31$ (a), the v_r velocity component at z-height $\bar{z} = 81$ (b), and the v_z velocity component at z-height $\bar{z} = 81$ (c) for the stratified molecular gas (case 2) in the same 10 representative r-stratification layers as in Figs. 6a, 7a, and 7c, respectively. Despite the fact that this "open orifice" pipe represents the case of minimum impedance for the flow (case 2), the radially driven gas inflow induced is still quite prominent (Figs. 9a and 9b).

downstream from it but also at considerable distances radially inward from it and at z-heights well above and below, is an important major characteristic common to all the hypersonic, stratified flows studied, regardless of whether the object is a flat plate, a "long" solid rod, or a "short," cylindrical pipe. In the case of the "short," cylindrical pipe, whose projected (effective obstructing) surface area normal to the incident flow can be varied, the radial inflow is still prominent even when the orifice in the pipe's downstream endplate is "fully open." This case of "fully open" orifice has a projected surface area normal to the incident flow of only a few percent (2%) the total pipe cross section, contributed entirely by the circumferential rim of the pipe, and represents the limiting case of "minimum gas impedance" (and maximum withdrawal of gas). Nevertheless the magnitude of the radial inflow induced is still 60% that in the limiting case of "maximum impedance" with orifice "completely closed."

The strong radial inflow is a striking "three-dimensional" effect induced when highly stratified gas impinges upon an obstacle. If it were not for the presence of the obstacle, the gas would undergo uniform rotation about the central z-axis of the cylindrical computational chamber. In such a situation, the pressure force of the radially inward directed pressure gradient that maintains the strong radial density stratification would be exactly in balance with the centrifugal force associated with purely circular motion of the gas. However, with the obstacle present, the gas is obstructed and undergoes strong deceleration in the circumferential direction of the mean flow; this induces a change in the radial balance of forces near the obstructing object. The centrifugal force of the decelerated gas is substantially reduced below that required to balance the strong, inward pressure gradient force of the otherwise [illegible] the highly stratified gas by the obstructing pipe that drives the strong inflow of gas radially inward.

A second major characteristic common to all the hypersonic, stratified flows studied is the striking "r-asymmetry" present in the resultant three-dimensional density distribution of the obstructed molecular gas. The space-averaged displacement of obstructed stratified gas is predominantly in one direction—the inward radial direction. Gas at higher r-stratification layers is redistributed to lower r-stratification layers in the vicinity of the obstacle (cf. Figs. 2b, 2c, and 8b). This is the case even for gas at radial locations greater than that of the pipe. The prominence of the "r-asymmetry" induced in the resultant density distribution is directly related to the strength of the pressure gradient-driven radial gas inflow (cf. Figs. 2b and 4d).

In contrast, a characteristic "z-symmetry" is manifested in the resultant three-dimensional density distribution about the $z=0$ midplane containing the central axis of the pipe (cf. Figs. 2a, 2c, 4a, and 8a). This "reflection symmetry" with respect to the z-direction is also a manifestation shared by the resultant velocity field of obstructed gas (cf. Figs. 4b, 4c, 5b, and 5c). Such "z-symmetry" constitutes a third major characteristic common to the hypersonic, stratified flows studied, for which the obstructing object itself is symmetric with respect to the $z=0$ midplane.

Deeper understanding can be achieved through comparisons of the hypersonic, stratified flows in cases 1 and 2, which are our primary focus in this paper, and corresponding hypersonic, "unstratified" flows, for which we have also carried out computational studies. In the "unstratified cases, the three-dimensional flow is directed along a rectilinear tube past the obstructing pipe. In the Cartesian geometry of the tube, the cylindrical pipe is aligned so that its central axis coincides with the mean flow direction along the tube. The computed results show that both r-θ and z-θ projections of the resultant gas density distribution exhibit reflection symmetry about the projected axis of the pipe and that the isodensity contours in an r-θ projected computational slice are closely coincident with those in a z-θ projected computational slice located at the same distance from the pipe's central axis. Indeed, the incident unstratified flow produces a resultant gas density distribution which exhibits rotation symmetry about the central axis of the pipe. To be sure, in an r-z projected computational slice just upstream of the pipe at the same location as that of Fig. 2c, the resultant density distribution for incident unstratified flow exhibits nearly circular isodensity contour levels centered on the pipe's central axis, quite different from the set of nearly vertical isodensity contours with inward-perturbed displacements for the stratified flows studied (cf. Fig. 2c). This is in striking contrast to the computed results for hypersonic, stratified flows which show that such "rotation-symmetry" about the pipe's central axis is washed away and transformed into "r-asymmetry" in the direction of the gradient of density stratification (Figs. 2b, 2c, and 8b). The magnitude of the "r-asymmetric" displacement of a contour level is proportional to the degree to which obstructed gas in that stratification layer is deflected radially inward by the strong radial pressure gradient.

It suffices to summarize the computed results for unstratified flows in one representative case, adopted as a "standard" of comparison: hypersonic, "unstratified" flow past the "short," cylindrical pipe with orifice in the downstream endplate "completely closed" (case 3). Neither a z-θ projection nor an r-θ projection of the gas density distribution for the unstratified flow is presented herein in a separate figure; contour levels in "both" types of projections for unstratified case 3 are nearly identical to those in equivalent z-θ projections for stratified case 1. For example, in a z-θ projection equivalent to that in Fig. 2a, the gas attains maximum and minimum densities at approximately the same locations respectively as for the stratified flow in case 1; the computed density contrast of 40.7 for the incident unstratified flow (case 3) is only slightly greater by a few percent (2–3%) than that factor of 39.8 in density contrast computed for the stratified flow (case 1). In a z-θ projected computational slice, equivalent to that in Fig. 4a, the computed density contrast is 2.92 in case 3, different by only a few percent (4%) from the corresponding value of 2.82 computed in case 1. Note though in this latter computational slice that the maximum and minimum (and average) densities are higher than those attained in stratified case 1 (Fig. 4a) by a factor of 2.86. This difference in molecular gas density between stratified and unstratified flows is attributed to the overall depletion of molecular gas within the stratification layer at $\bar{r} = 735$ in stratified case 1, resulting from the large radial inflow induced in the stratified molecular gas there that carries a significant fraction of the gas to inner radial locations.

For the unstratified flow in case 3, the "bow shock" and "density ridge" exhibit the characteristic shape of a paraboloid of revolution with principal axis of rotation-symmetry coincident with the central axis of the pipe. In a z-θ projected computational slice at average radius $\bar{r} = 735$, equivalent to that in Fig. 4a, this bow shock and density ridge bend downstream less rapidly, making an oblique angle of magnitude close to 45° with respect to the θ-direction at the upper and lower boundaries ($\bar{z} = \pm 94$), as compared to that of 30° for the stratified flow in case 1. Note in an r-θ computational slice, such as that in Figs. 2b and 8b, that this bow shock and density ridge for the stratified flow are largely washed out and masked against the strongly stratified density background.

Comparisons of the velocity fields in the stratified and unstratified cases further emphasize the similar common characteristics as well as the important differences. The velocity field for unstratified flow (case 3) exhibits rotation symmetry about the central axis of the pipe. The component of velocity perpendicular to the pipe's central axis, and directed outward from it, attains its maximum values along the paraboloid-shaped oblique bow shock and density ridge, which engulfs the pipe from the upstream direction and whose axis of revolution lies coincident with the pipe's central axis. Isovelocity contour maps for the unstratified flow in z-θ projected computational slices reveal isovelocity contours closely coincident with those in corresponding z-θ computational slices for the stratified flow (e.g., Fig. 4b). The magnitudes of the maximum and minimum v_z velocities ($v_{z_{\max}} = 2.58$ and $v_{z_{\min}} = -2.42$), attained along the oblique bow shock and density ridge just above and below the pipe, respectively, are somewhat lower by approximately 75% than those for the stratified flow in the z-θ projected computational slice in Fig. 4b ($v_{z_{\max}} = 3.27$ and $v_{z_{\min}} = -3.44$). In striking contrast, the v_r velocity field for the stratified flow attains its greatest negative values along a locus that extends almost radially inward from the front end of the pipe. The locus of greatest negative (v_r/v_θ) values makes an angle of 75°–90° with respect to the θ direction, all the way inward to a radial position of 620 units, with little or no bending into an oblique orientation, unlike that oblique shock for the computed unstratified flow (case 3). Note that the flow is redirected sharply inward in passage across this "shock" locus (cf. Figs. 4d and 5a), even though the corresponding density enhancement across the locus is largely masked within the strongly stratified density background.

These studies of hypersonic gas flows past an obstacle in a rarefied, strongly stratified medium have been made possible through the development of our "N-body" computational code based on Monte Carlo techniques. Improvements in the computational code over an earlier version described by Hausman and Roberts [4] include: (i) refinements toward more realistic hypersonic, rotating, stratified flows as well as hypersonic non-rotating, unstratified flows, (ii) the formulation of the computational problem for rotating, stratified flows in terms of cylindrical coordinates instead of Cartesian coordinates, (iii) the replacement of artificially simulated centrifugal forces (in Cartesian geometry) by appropriate inclusion of such forces for the rotating, stratified flows, (iv) variable computational cell volumes for higher resolution in selected regions near the obstacle, and (v) improved treatment of the physical boundary conditions. The "N-body" computational code exhibits capabilities beyond currently available continuum codes in simulating the flows in rarefied and quasi-rarefied/continuum regimes, and our present study exploits these unique capabilities to describe the stratified gas flows in and around representive obstacles in these flow regimes. The "short" cylindrical pipe, with open end facing directly into the flow serves as a useful model of impact probes and scoops in gas centrifuges.

The complicated nature of the strongly stratified gas flows studied in this paper, quite apart from its details, indicates that short scale height systems interacting with finite-sized solid obstacles cannot be effectively modeled in detail by two-dimensional calculations. Figures 2a–2c, 3a, 3b, 4a, 8a, and 8b demonstrate how the density varies independently in all directions and shows no simplifying symmetries which might allow the problem to be recast into two dimensions. Perhaps the most obvious "three-dimensional" effect of the interaction of short scale heights with intermediate mean free paths is the net inward motion of the scattered gas. We have seen in regions inward of the pipe that the velocity is more nearly radial than axial (cf. Figs. 4b–4d, 5a, 5c, 6a, 6c, 7a, 7c, and 9a–9c).

Based upon the results of our simulations, we have predicted several general effects that obstructed flow in a highly stratified medium might produce. Are these predictions subject to experimental test? The local density perturbations of the molecular gas shown in Figs. 2a–2c, 3a, 3b, 4a, 8a, and 8b might in fact be very difficult to map in a real system. The exponential dependence upon radial location tends to mask all but the strongest perturbations (cf. Figs. 2b, 2c, and 8b), unless extremely accurate positioning is available for quite small measuring devices. The velocity fields hold out more hope, however. In particular, the radial motion (cf. Figs. 4c, 4d, 5a, 5c, 6a, 7a, 9a, and 9b) of the inward-driven gas and corresponding radial mass flux are important model results for which unambiguous tests should be possible. To be sure, the effects of a somewhat larger obstacle (compared to either gas scale height or collisional mean free path) would be expected to enhance these systematic motions as well as the density perturbations induced in the gas.

We believe that the computational algorithm adopted for our simulations, based on Monte Carlo particle dynamics, is a good choice for modeling the intermediate-λ regime of interest here. The main problems arising from its use are spatial resolution and computer time requirements. The computational cells used to predict particle collision rates, local density, and velocity fields are of size $25 \times 25 \times 12.5$ ($r \times \theta \times z$, units^3) in regions where the highest cellular resolution is desired, only a factor 4 to 8 times smaller along an edge than the diameter and length of the pipe itself (both 100 units). In a short-λ gas this would give ample reason to fear that we are washing out small-scale structure and smoothing our shocks. However, we have seen that much of the interesting, potentially observable structure is found at radii inward from the pipe, where the collisional mean free path λ is 20 units or longer (much longer in the innermost *r*-layers; e.g., $\lambda_{\text{unperturbed}} = 516$ units in the *r*-stratification layer at $\bar{r} = 616$). We assert that the gas cannot show meaningful structure on scales much smaller than the lesser of λ or H, and that our spatial resolution is therefore adequate for these regions. We predict, therefore, that the high-density ridges seen in the computations are probably not narrow shocks and very likely look much as we have depicted them.

However, the mean free path is much shorter than 20 units in the outermost *r*-stratification layers. It is certainly possible that structure should develop here which is much smaller than our cell sizes and is smoothed into invisibility by the course grid. Related to this is the fact that the collision time scale in these cells is much shorter than our computational time steps, so most particles near the outer boundary can be expected to experience several collisions per time step. These will completely randomize and isotropize particle velocity dispersions while preserving the mass, momentum, and energy of each cell as a whole. But this is just the effect we expect in this short-λ, near-continuum regime, so the high collision rate apparently introduces no new biases (as long as we are simulating only time-invariant models).

Because of the large cell sizes (compared to λ) in the outermost *r*-stratification layers, we are not confident that the relative smoothness of these outer regions is realistic. Simulations with much smaller cell sizes here, and consequently larger numbers of particles, would be required to confirm or deny our results. Nevertheless, where we "do" see structure, at the radial location of the pipe and inward, the mean free path is long enough and the collision rate small enough that we feel confident of having an accurate portrayal.

A problem common to all particle representations of gases is that estimates of density, velocity, etc., in any volume element are subject to Poisson statistics with relative error proportional to the inverse square root of particle number. Good determination of local values, therefore, demands very many model particles. Unlike deterministic particle-collision models, whose computation time goes up with the square of particle number, the Monte Carlo method described in Section II requires computation time linearly proportional to particle number (if the mean free path is fixed). If the system modeled is time-independent, we can get equivalent statistics (and computation time) by putting a great many particles into the system at once or integrating the effects of fewer particles over numerous time steps (the approach taken here). This is strictly true only if the number of particles is sufficient that a statistically significant number of collisions occurs in each cell during each time step. Toward the very inner radii of the computational volume, this may not be the case.

The computation time of the Monte Carlo algorithm is proportional to the collision rate per molecule, which can get uncomfortably high at the outer edge of a short scale height model. As a consequence, the Monte Carlo particle dynamics approach seems limited to regions 10 or fewer scale heights across, inadequate to model an entire gas centrifuge, for example. However, the high collision rate regime is precisely where the standard equations of hydrodynamics become appropriate, so it may be possible to write a hybrid computer algorithm, which uses regular hydrodynamics in high density regions and particle dynamics in lower density regions. We also speculate that model "impact probes" and "scoops" of more realistically intricate geometries and shapes than the "short," cylindrical pipe studied here (with adjustable diameter of orifice in the downstream endplate) may be computationally feasible and might lead to still more complex and interesting predictions.

APPENDIX

After making the molecule-to-particle substitutions [Eq. (6)], we derive the rate at which particles flow into each block of equal-sized cells which lie along the outermost ($r = \text{constant} \equiv R$) boundary of our volume:

$$\frac{\Delta N_p}{\Delta t} = n_z n_\theta k' \frac{\Omega^2 R}{\sqrt{2\pi}\, v_d} \frac{\exp(\Omega^2 R^2/2v_d^2)}{[\exp(\Omega^2 R^2/2v_d^2) - \exp(\Omega^2 r_{\text{in}}^2/2v_d^2)]}, \tag{A1}$$

where n_z and n_θ are the number of z divisions and θ divisions, respectively, which divide the block into cells, k' is the desired average number of particles per cell, and r_{in} is the radius of the inner boundary of *that block* of cells (not the inner boundary of the whole computational region). The θ and z coordinates at which each particle passes the ($r = R$) boundary may be randomly chosen between the upper and lower limits which define the cell-block's θ and z boundaries. The θ and z velocity components of each entering particle are determined from normally distributed random numbers with standard deviations of v_d and mean values of ΩR and 0, respectively. The r velocity component of each entering particle is randomly chosen by integrating and inverting Eq. (10) with $s = 0$:

$$v_r = -v_d \sqrt{-2 \ln R_f}, \tag{A2}$$

where R_f is a random number chosen from a uniform distribution between 0 and 1.

At the innermost boundary, where $r = r_{\min}$, a similar input rate formula holds for each block of identical cells:

$$\frac{\Delta N_p}{\Delta t} = n_z n_\theta k' \frac{\Omega^2 r_{\min}}{\sqrt{2\pi}\, v_d} \frac{\exp(\Omega^2 r_{\min}^2/2v_d^2)}{[\exp(\Omega^2 r_{\text{out}}^2/2v_d^2) - \exp(\Omega^2 r_{\min}^2/2v_d^2)]}, \tag{A3}$$

where r_{out} is the outer r boundary of this cell-block. The r, θ, and z components of input velocity for each new particle are chosen as described above, except that the mean θ velocity is $\Omega r_{\min}$ and v_r is always *positive.*

For blocks of cells facing the top or bottom boundaries of our volume ($z = z_{\max}$ or $z = z_{\min}$), the particle input rate is simply expressed:

$$\frac{\Delta N_p}{\Delta t} = \frac{n_\theta k' v_d}{\sqrt{2\pi}\, \Delta z_c}, \tag{A4}$$

where Δz_c is the z-height of any single cell in the block. The θ coordinate at which each particle crosses the z boundary can again be randomly chosen between the θ limits of the block, but the r coordinate must be weighted toward high values to reflect the radial dependence of the incoming flux. It turns out that, in order to reproduce the density distribution of Eq. (5) for incoming particles, each particle's radial location should be chosen by the algorithm

$$r = \frac{\sqrt{2}\, v_d}{\Omega} \left[\ln\left\{ R_f\left[\exp(\Omega^2 r_{\text{out}}^2/2v_d^2) - \exp(\Omega^2 r_{\text{in}}^2/2v_d^2)\right] + \exp(\Omega^2 r_{\text{in}}^2/2v_d^2)\right\}\right]^{1/2}, \tag{A5}$$

where R_f is a random number from a $[0, 1]$ uniform distribution, and r_{in} and r_{out} are the inner and outer radii of this cell block. After r is chosen, the θ and r velocity components are chosen from normal distributions with standard deviations v_d and mean values Ωr and 0, respectively. The z velocity is given by Eq. (A2), with the sign chosen to assure that the new particles are entering, not leaving the boundary.

Blocks of cells facing the upstream boundary ($\theta = \text{constant} = \theta_{\text{min}}$) experience a particle inflow rate calculated from

$$\begin{aligned}\frac{\Delta N_p}{\Delta t} = \frac{\Omega n_z k'}{2\,\Delta\theta_c} &\left\{\exp(\Omega^2 r_{\text{out}}^2/2v_d^2)\left[1 + \operatorname{erf}(\Omega r_{\text{out}}/\sqrt{2}\, v_d)\right]\right. \\ &\left. - \exp(\Omega^2 r_{\text{in}}^2/2v_d^2)\left[1 + \operatorname{erf}(\Omega r_{\text{in}}/\sqrt{2}\, v_d)\right]\right\} \\ &\times \left[\exp(\Omega^2 r_{\text{out}}^2/2v_d^2) - \exp(\Omega^2 r_{\text{in}}^2/2v_d^2)\right]^{-1},\end{aligned} \tag{A6}$$

where $\Delta\theta_c$ is the θ-length of each cell in the block. The z coordinate at which each particle crosses the θ_{min} boundary may be randomly chosen between the block's z-limits. It is more complicated to choose the radius of incoming particles. If we define $x = \Omega r/\sqrt{2}\, v_d$, the radial distribution of particles entering the upstream face is proportional to

$$f(x)\, dx \propto \left[1 + \sqrt{\pi}\, x \exp(x^2)(1 + \operatorname{erf} x)\right] dx. \tag{A7}$$

This expression cannot be integrated and inverted analytically, so values of x, and hence r, must be chosen by acceptance–rejection methods. Once we choose r, the distribution of probable θ velocity components is given by

$$f(v_\theta)\, dv_\theta \propto |v_\theta| \exp\left[-(v_\theta - \Omega r)^2/2v_d^2\right] dv_\theta. \tag{A8}$$

This also is uninvertible, and v_θ must also be chosen by acceptance–rejection methods. The r and z velocity components are both normally distributed around means of 0 with standard deviations of v_d.

Usually, very few particles can be expected to enter the downstream face ($\theta = \theta_{\text{max}}$) of the computational volume. The input rate is given by the formula

$$\begin{aligned}\frac{\Delta N_p}{\Delta t}=\frac{\Omega n_z k'}{2\,\Delta\theta_c}&\{\exp(\Omega^2 r_{\text{in}}^2/2v_d^2)[1-\mathrm{erf}(\Omega r_{\text{in}}/\sqrt{2}\,v_d)]\\&-\exp(\Omega^2 r_{\text{out}}^2/2v_d^2)[1-\mathrm{erf}(\Omega r_{\text{out}}/\sqrt{2}\,v_d)]\}\\&\times[\exp(\Omega^2 r_{\text{out}}^2/2v_d^2)-\exp(\Omega^2 r_{\text{in}}^2/2v_d^2)]^{-1}.\end{aligned}\tag{A9}$$

If this rate is not negligibly small for a given block of cells facing the downstream boundary, the coordinates and velocities of the new particles are chosen by the same methods described for the upstream face, except the expression which must be used to choose r (again by acceptance–rejection methods) is

$$f(x)\,dx \propto [1-\sqrt{\pi}\,x\exp(x^2)(1-\mathrm{erf}\,x)]\,dx. \tag{A10}$$

The inner r boundary of our computational volume may be treated one of three ways: an open surface with inward flux as just described (and adopted in most of the cases considered), a surface of zero area as r_{min} goes to zero (with no flux in or [illegible] might undergo rapid rotation (e.g., as in a gas centrifuge). The solid surface is assumed to be a non-rotating diffuse scatterer; that is, all particles which strike it are reemitted in a new, randomly chosen direction, with no mean rotation, and velocities chosen appropriate to the surface's temperature, which need not equal the rotating gas's temperature.

ACKNOWLEDGMENTS

This work was supported in part by the Department of Energy under Grant DE-AC05-820R20900. The early development of the computational method for application to research on galactic systems and planetary systems was also supported in part by the National Science Foundation under Grants AST-79-09935 and AST-82-04256 and the National Aeronautics and Space Administration under Grant NASA-NAGW-929.

REFERENCES

1. G. A. BIRD, *Phys. Fluids* **13**, 2676 (1969).
2. G. A. BIRD, *Molecular Gas Dynamics* (Clarendon Press, Oxford, 1976), Chaps. 6, 7, 9, and 10, and Appendices D, F, G, and H.
3. G. A. BIRD, Department of Aeronautical Engineering, University of Sydney, Sydney, Australia, private communication (1986).
4. M. A. HAUSMAN AND W. W. ROBERTS, JR., *J. Comput. Phys.* **55** 347 (1984).
5. W. W. ROBERTS, JR. AND M. A. HAUSMAN, in *Proceedings of the Sixth Workshop on Gases in Strong Rotation, Tokyo, Japan, 1985*, edited by Y. Takashima (Saitama University, Tokyo, 1986), p. 115.